Article:

Bosmans, JHC, Erb, MP, Dolan, AM orcid.org/0000-0002-9585-9648 et al. (6 more authors) (2018) Response of the Asian summer monsoons to idealized precession and obliquity forcing in a set of GCMs. Quaternary Science Reviews, 188. pp. 121-135. ISSN 0277-3791

https://doi.org/10.1016/j.quascirev.2018.03.025

x

Response of the Asian summer monsoons to idealized precession and obliquity forcing in a set of GCMs

J.H.C. Bosmans[a,1,*], M.P. Erb[b,2,3], A.M. Dolan[c], S. S. Drijfhout[d,4,5], E. Tuenter[d,6], F.J. Hilgen[a], D. Edge[c], J.O. Pope[c,7], and L.J. Lourens[a]

[a]Utrecht University, Faculty of Geosciences, Postbus 80.115, 3508 TC, Utrecht, Netherlands
[b]School of Earth Sciences and Environmental Sustainability, Northern Arizona University, Flagstaff, Arizona
[c]School of Earth and Environment, University of Leeds, Leeds LS2 9JT, UK
[d]Royal Netherlands Meteorological Institute, Postbus 201, 3730 AE, De Bilt, Netherlands
[1]Formerly also at: Royal Netherlands Meteorological Institute[d]
[2]Formerly at: Department of Earth Sciences, University of Southern California, Los Angeles, California
[3]Formerly at: Institute for Geophysics, University of Texas at Austin, 10100 Burnet Road (R2200) Austin, TX 78758-4445, Texas, USA
[4]Currently also at: University of Southampton, Ocean and Earth Sciences, Waterfront Campus (NOCS), European Way, Southampton SO14 3ZH, United Kingdom
[5]Utrecht University, Faculty of Science, Princetonplein 5, 3584 CC, Utrecht, Netherlands
[6]Formerly also at: Utrecht University, Faculty of Geosciences[a]
[7]Currently at: British Antarctic Survey, Cambridge, UK
*Corresponding author, J.H.C.Bosmans@UU.nl

March 5, 2018

Abstract

We examine the response of the Indian and East Asian summer monsoons to separate precession and obliquity forcing, using a set of fully coupled high-resolution models for the first time: EC-Earth, GFDL CM2.1, CESM and HadCM3. We focus on the effect of insolation changes on monsoon precipitation and underlying circulation changes, and find strong model agreement despite a range of model physics, parameterization, and resolution. Our results show increased summer monsoon precipitation at times of increased summer insolation, i.e. minimum precession and maximum obliquity, accompanied by a redistribution of precipitation and convection from ocean to land. Southerly monsoon winds over East Asia are strengthened as a consequence of an intensified land-sea pressure gradient. The response of the Indian summer monsoon is less straightforward. Over south-east Asia low surface pressure is less pronounced and winds over the northern Indian Ocean are directed more westward. An Indian Ocean Dipole pattern emerges, with increased precipitation and convection over the western Indian Ocean. Increased temperatures occur during minimum precession over the Indian Ocean, but not during maximum obliquity when insolation is reduced over the tropics and southern hemisphere during northern hemisphere summer. Evaporation is reduced over the northern Indian Ocean, which together with increased precipitation over the western Indian Ocean dampens the increase of monsoonal precipitation over the continent. The southern tropical Indian Ocean as well as the western tropical Pacific (for precession) act as a moisture source for enhanced monsoonal precipitation. The models are in closest agreement for precession-induced changes, with more model spread for obliquity-induced changes, possibly related to a smaller insolation forcing. Our results indicate that a direct response of the Indian and East Asian summer monsoons to insolation forcing is possible, in line with speleothem records but in contrast to what most marine proxy climate records suggest.

Keywords: monsoon, orbital forcing, paleoclimate modeling, South-East Asia, multi-model, climate dynamics

1 Introduction

Monsoon systems play a key role in Asian climate, representing a strong seasonal climate signal over an area spanning from the Arabian to the Chinese Seas. The summer monsoon onset occurs in late spring / early summer for the East Asian monsoon, and in summer for the Indian monsoon, when the Intertropical Convergence Zone (ITCZ) rapidly moves northward towards the continent, conveying large amounts of moisture and energy (e.g. Bordoni and Schneider, 2008; Molnar et al., 2010; Mohtadi et al., 2016). On time scales of 10^3-10^5 years, the Asian monsoons are dominated by changes in the distribution of incoming solar radiation, the orbital or so-called Milankovitch cycles. This cyclic variation in the spatial and temporal distribution of radiation has a strong influence on Earth's climate (e.g. Ruddiman, 2006b; Mohtadi et al., 2016). Precession controls the seasonality of insolation at all latitudes and is modulated by the eccentricity of the earth's orbit, while obliquity (tilt) affects mostly high latitude summer insolation and meridional insolation gradients. All three orbital parameters (precession, eccentricity, and obliquity) are observed in proxy climate records of monsoon strength. Examples of such records are oxygen isotope speleothem records from east China (e.g. Wang et al., 2008) as well as India (e.g. Kathayat et al., 2016), dominated by precession cyclicity, as well as the multi-proxy stack of Indian summer monsoon circulation strength from the western Arabian Sea, where southwesterly summer monsoon winds influence upwelling, productivity and sedimentation (e.g. Clemens and Prell, 2003). The latter shows a strong obliquity signal as well, despite the dominance of precession in low-latitude summer insolation.

Despite the remaining controversies in the interpretation of oxygen isotope speleothem records (e.g. Caley et al., 2014; Mohtadi et al., 2016) the strong precession signal in phase with insolation in Chinese and Indian speleothem records (e.g. Wang et al., 2008; Cai et al., 2015; Kathayat et al., 2016) is in line with climate model simulations (e.g. Battisti et al., 2014; Rachmayani et al., 2016). The interpretation of the Arabian Sea proxies, originally thought to show a long lag of monsoon strength with respect to precession (e.g. Clemens and Prell, 2003), also remains an item of discussion (e.g. Ziegler et al., 2010; Caley et al., 2011), with a recent modeling study suggesting that Arabian Sea productivity, part of the multi-proxy stack, is not necessarily enhanced at times of a stronger Indian Summer Monsoon (Le Mézo et al., 2016). This could explain the discrepancy in lags between proxy studies and speleothem records as well as modeling studies, with the latter showing no lags. Modelling studies corroborate the strengthening of summer monsoons at times of orbitally forced high summer insolation and the weakening at times of orbitally forced weak insolation, even if experiments are run for only up to a few hundred years (i.e. short on the orbital time scale). In some of the earliest paleoclimate modelling studies, atmosphere-only models showed a strengthened thermal low over the continents and a stronger land/sea thermal contrast, causing increased summer monsoon precipitation at times of high summer insolation (e.g. Kutzbach and Otto-Bliesner, 1982; Kutzbach and Guetter, 1986; Prell and Kutzbach, 1987). More recently several studies of the Mid-Holocene, a time of enhanced Northern Hemisphere insolation seasonality, were performed within the framework of the Paleoclimate Modelling Intercomparison Project (PMIP, Braconnot et al. (2007)). During the Mid-Holocene, models show a stronger Indian Summer Monsoon (ISM) and East Asian Summer Monsoon (EASM). The EASM strengthening is related to a stronger land/sea pressure gradient (Jiang et al., 2013; Wang and Wang, 2013; Zheng et al., 2013). Strengthening of the ISM may be affected by mechanisms such as the Indian Ocean Dipole (Zhao et al., 2005; Abram et al., 2007). Other studies of periods with a precession-induced increase in insolation seasonality have also demonstrated a strengthening of the ISM (Braconnot and Marti, 2003; Braconnot et al., 2008; Battisti et al., 2014; Araya-Melo et al., 2015; Rachmayani et al., 2016).

Only a few studies have investigated the separate precession and obliquity forcing instead of focusing on a specific time with combined precession and obliquity forcing. Tuenter et al. (2003) showed a deepening of the convergence zone over southern Asia and increased summer precipitation over the Asian monsoon regions during both minimum precession and maximum obliquity (both times of increased summer insolation). However, we have already shown that the mechanisms behind the response to orbital forcing in their model is rather different from the response in the EC-Earth model used here, specifically for the North African monsoon Bosmans et al. (2015a). Nonetheless, the orbitally induced changes in precipitation are similar to those identified by Erb et al. (2013). Mantsis et al. (2013) report increased precipitation during minimum precession as well, which for East Asia is related to reduced pressure over land as well as an increased North Pacific high pressure area, both intensifying the land/sea pressure gradient. This is also modeled by Shi et al. (2011) for both precession and obliquity and by Wang et al. (2012) for precession. Chen et al. (2011b) focus solely on obliquity, showing that the ISM and the South-EASM are stronger during maximum obliquity, while the North-EASM is weaker. Wu et al. (2016) show that high obliquity during the early Holocene augments the impact of precession by affecting high pressure systems and meridional gradients in pressure and temperature. Multiple studies have found that the orbital-induced changes in surface pressure over the South Asian monsoon regions do not show a straightforward change in land/sea pressure differences (Zhao et al., 2005; Chen et al., 2011b; Mantsis et al., 2013).

The link between orbitally forced changes in insolation and monsoon strength has thus been established by both proxy climate records and modelling studies. Here, we focus on the mechanisms behind changes in summer monsoon strength using state-of-the-art general circulation models, assessing the detailed pattern of the ISM and EASM response to both precession and obliquity forcing using fully coupled general circulation models (EC-Earth, GFDL, CESM for precession and obliquity as well as HadCM3 for obliquity). These models cover a range of model physics, parameterization and resolution. Such a multi-model approach provides the opportunity to judge whether results are model-dependent, and if this is not the case, provides robust mechanisms behind the orbital signals observed in proxy records. We single out the effects of precession and obliquity, as the latter has a relatively strong impact on monsoon strength given its weak impact on low-latitude insolation (e.g. Tuenter et al., 2003). Using idealized experiments enables us to separate and maximize the precession and obliquity signals in our experiments.

This paper is organised as follows: Section 2 describes each of the general circulation models and the experimental set-up. Section 3 shows the changes in monsoon precipitation and associated circulation, with Section 3.1 focusing on precession and Section 3.2 focussing on obliquity. A discussion and conclusion are given in Sections 4 and 5.

2 Model and Experiment set-up

2.1 EC-Earth

EC-Earth is a fully coupled ocean-atmosphere GCM (general circulation model, Hazeleger et al. 2010, 2011). The atmospheric part of EC-Earth 2.2 is based on the Integrated Forecasting System (IFS), cycle 31R1, of the European Centre for Medium-range Weather Forecast (ECMWF). Its horizontal resolution is T159 (roughly 1.125° x 1.125°) with 62 vertical levels. The ocean model NEMO runs at a resolution of nominally 1° with 42 vertical levels. The ocean, ice, land and atmosphere are coupled through the OASIS3 coupler (Valcke and Morel, 2006).

EC-Earth has previously been shown to represent monsoons well in both the pre-industrial and the Mid-Holocene paleo-experiment (Bosmans et al., 2012). Furthermore, the orbital extreme experiments used in this paper were also used to investigate orbital forcing of the North-African monsoon (Bosmans et al., 2015a).

2.2 GFDL CM2.1

The GFDL CM2.1 model is the Geophysical Fluid Dynamics Laboratory Climate Model version 2.1, (Delworth et al., 2006). Like EC-Earth 2.2 this is an ocean-atmosphere fully coupled model, including land and sea ice components. It runs at a resolution of 2° latitude by 2.5° longitude with 24 vertical levels and an ocean resolution of 1° x 1°, with higher meridional resolution near the equator, and 50 vertical levels. The atmospheric model has a time step of 3 hours for radiation and 30 min for other atmospheric physics.

GFDL-CM2.1 has previously been used to investigate climatic response to orbital forcing (e.g. Mantsis et al., 2013). The orbital experiments used here are the same as in Erb et al. (2015), where the climatic response to changes in obliquity, precession, CO_2 and ice sheets is investigated. Here we use the orbital experiments with pre-industrial greenhouse gas concentrations and ice sheets.

2.3 CESM

The GFDL experiments were repeated with the National Center for Atmospheric Research's (NCAR) Community Earth System Model 1.2 (CESM1.2), which is also a fully coupled atmosphere-ocean model. CESM1.2 includes the CAM5 Community Atmospheric Model at 2.5 x 1.875 resolution with a 30 minute time step and 30 vertical levels, the POP2 Parallel Ocean Program as the oceanic component, running at approximately 1 x 0.5 resolution with 60 vertical levels, and the Community Land Model CLM4.0. Fixed vegetation is used. Here we use the same idealized simulations previously used to study the climate response to changes in obliquity and other past forcings (Erb et al., 2018).

2.4 HadCM3

HadCM3 is the UK Met Office Hadley Centre Coupled Climate Model Version3. Its horizontal resolution of the atmosphere model is 2.5° in latitude by 3.75° in longitude and consists of 19 layers in the vertical, comparable to a T42 spectral model resolution. The atmospheric model has a time step of 30 min. The spatial resolution over the ocean is 1.25° x 1.25° with 20 vertical layers. The sea-ice model uses a simple thermodynamic scheme and contains parameterisations of ice drift and leads (Cattle et al., 1995).

HadCM3 is well documented (Gordon et al., 2000) and has previously been shown to reproduce the main features of modern climate observations. Furthermore, HadCM3 has been used in the past to examine the effect of orbital forcing in the Quaternary (e.g. Singarayer and Valdes, 2010) and in earlier periods such as the mid-Pliocene (e.g. Dolan et al., 2011; Prescott et al., 2014).

2.5 Experimental set-up: insolation forcing and boundary conditions

This study is based on experiments of orbital extremes, with EC-Earth, GFDL-CM2.1 and CESM running both precession and obliquity extremes and HadCM3 running the obliquity extremes. These model simulations form an ensemble of opportunity rather than being part of a pre-defined model intercomparison project. As a result, there are small differences in the experimental design. The main differences between the experiments in all models are the orbital parameters, and thus the insolation forcing, but there are small differences in the exact orbital parameters and greenhouse gas concentrations. Generally, EC-Earth and HadCM3 have the same set-up, as do GFDL-CM2.1 and CESM. Table 1 shows the set-up per experiment and per model. Four time-slice experiments are performed to examine the separate precession and obliquity signals: minimum and maximum precession (Pmin and Pmax) as well as maximum and minimum obliquity (Tmax and Tmin, T for tilt), allowing us to maximize the orbital signals from our experiments. All simulations are performed with fixed present-day ice sheets and vegetation.

During a precession minimum (Pmin) the summer solstice (midsummer) occurs at perihelion (the point in the earth's orbit closest to the Sun), so seasonality is enhanced on the Northern Hemisphere and reduced on the Southern

Table 1: Overview of the orbital configuration in each experiment. Obl is the obliquity (tilt, in degrees), $\tilde{\omega}$ is the longitude of perihelion, defined here as the angle from the vernal equinox to perihelion in degrees, measured counterclockwise. e is eccentricity. $e\ \sin(\pi+\tilde{\omega})$ is the precession parameter. Note that for Tmax and Tmin there is no precession when a circular orbit (e=0) is used. For GHGs the year of the greenhouse gas concentrations is given, with the CO_2 concentration in parentheses in ppmv. Calendar anchor point is either vernal equinox (v.e.), autumnal equinox (a.e.) or not applicable (n.a.) when e=0. An asterix (*) indicates that the model output has been processed onto a fixed-angular calendar.

	Obl (°)	$\tilde{\omega}$ (°)	e	$e\ \sin(\pi+\tilde{\omega})$	GHGs	Calendar anchor point
Pmax (perihelion at NH winter)						
EC-Earth	22.08	273.50	0.058	0.058	1850 (284.5)	v.e.
GFDL-CM2.1	23.439	270	0.0493	0.0493	1860 (286)	a.e.*
CESM	23.439	270	0.0493	0.0493	1860 (286)	v.e.*
Pmin (perihelion at NH summer)						
EC-Earth	22.08	95.96	0.056	-0.055	1850 (284.5)	v.e.
GFDL-CM2.1	23.439	90	0.0493	-0.0493	1860 (286)	a.e.*
CESM	23.439	90	0.0493	-0.0493	1860 (286)	v.e.*
Tmax (maximum obliquity)						
HadCM3	24.45	-	0	0	1850 (284.5)	n.a.
EC-Earth	24.45	-	0	0	1850 (284.5)	n.a.
GFDL-CM2.1	24.480	282.93	0.0167	0.0163	1860 (286)	a.e.
CESM	24.480	282.93	0.0167	0.0163	1860 (286)	v.e.
Tmin (minimum obliquity)						
HadCM3	22.08	-	0	0	1850 (284.5)	n.a.
EC-Earth	22.08	-	0	0	1850 (284.5)	n.a.
GFDL-CM2.1	22.079	282.93	0.0167	0.0163	1860 (286)	a.e.
CESM	22.079	282.93	0.0167	0.0163	1860 (286)	v.e.

Hemisphere. The opposite occurs during a precession maximum (Pmax), when winter solstice occurs at perihelion. In the obliquity experiments, eccentricity is set to zero to completely eliminate the effect of precession in EC-Earth and HadCM3, a small value of eccentricity is used in GFDL-CM2.1 and CESM. During an obliquity maximum (Tmax, T for tilt), both northern and southern hemisphere (NH, SH) summers receive more insolation, especially at the poles, while during an obliquity minimum (Tmin) summer insolation is reduced. Within one season, precession has the same effects on both hemispheres, while obliquity has the opposite effect. The values of the orbital parameters in each experiment are given in Table 1. For EC-Earth and HadCM3 these are the same as the P-T-, P+T-, P0T+, P0T- experiments in Tuenter et al. (2003), and are based on the most extreme values of the orbital parameters occuring in the last 1 Ma (Berger, 1978).

Insolation differences at $\sim$40°N can be as large as 100 Wm^{-2} for precession and 20 Wm^{-2} for obliquity (Figure 1). Note that the insolation change between the orbital extremes vary amongst the models due to slight differences in the orbital parameters, as well as the choice of calendar. For experiments in which eccentricity is not set to zero, the way the calendar is implemented can result in changes in the timing of the equinoxes and solstices, which may affect model results. In the EC-Earth precession experiments the vernal equinox is fixed at March 21st and the present-day calendar is used. The same applies to CESM, while GFDL-CM2.1 fixes the autumnal equinox at September 21st. Both the CESM and GFDL-CM2.1 monthly output is then corrected to fixed-angular "months" following Pollard and Reusch (2002) in order to account for this calendar effect (Erb et al., 2015). Figure A.1 shows the difference in the insolation changes. Studies have found that the calendar-effect has only a minor effect on the results (e.g. Chen et al., 2011a), also in HadCM3 seasonal results (Marzocchi et al., 2015). Here, we also find that for CESM and GFDL the results shown in this paper are not changed by the choice of calendar. Only the annual cycle changes slightly, but the patterns of change in summer that we focus on here remain the same, see Figures A.2, A.3, A.4. Despite the small differences in imposed forcings and calendars, we find that monsoonal responses are robust amongst models, further suggesting that the results are not overly sensitive to the exact experimental design.

In this study we compare Pmin to Pmax, and Tmax to Tmin, i.e. we investigate the effect of increased summer and decreased winter insolation on the Northern Hemisphere. EC-Earth experiments were run for 100 years, of which the last 50 years are used to create the climatologies shown in this study. This is long enough for top-of-atmosphere net radiation as well as atmospheric and surface variables that are of interest to equilibrate to the forcing (see Bosmans et al. (2015a)). The globally averaged tendency term of surface air temperature, dT/dt, is near-zero and shows no trend in all experiments (not shown). HadCM3 was run for 300 years per experiment, of which the last 50 years are used. GFDL-CM2.1 and CESM were run for at least 600 and 500 years respectively and 100-year climatologies were computed.

3 Results

In this section we first investigate the precession-induced changes in the Asian monsoons (Section 3.1), followed by the obliquity-induced changes (Section 3.2). We compare maximum to minimum NH summer insolation, i.e. Pmin to Pmax and Tmax to Tmin, using JJA averages. Precipitation results are shown for all models, other variables are shown for EC-Earth only for brevity. Results of all models are shown in the supplementary material (Section C).

3.1 Precession

Within the experiments presented here, the precession-induced insolation change reaches 100 Wm^{-2} in June (Figure 1) (Tuenter et al., 2003; Bosmans et al., 2015a). The JJA averaged insolation between 10°N and 40°N is $\sim$80 Wm^{-2} higher during Pmin than Pmax. Figure 2 shows that the average summer precip-

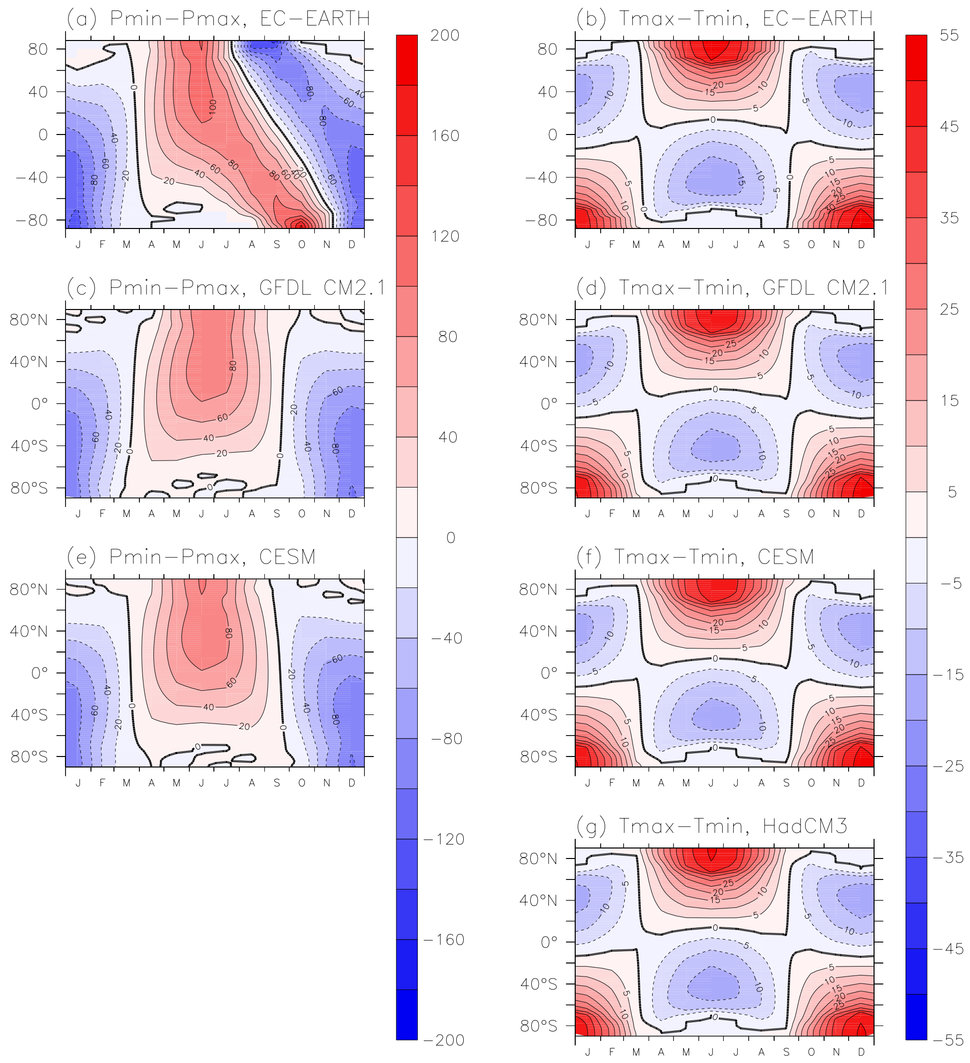

Figure 1: Insolation changes in W/m^2 per model and for the precession and obliquity experiments. See Table 1 for details on the orbital configuration per experiment. Note that output of the CESM and GFDL precession experiments has been processed onto a fixed-angular calendar, explaining the difference in precession-induced insolation change compared to EC-Earth, whose output remained on the fixed-day calendar used in the experiment. The range of insolation difference for precession (up to ∼100 W/m^2) is much larger than for obliquity (up to ∼50 W/m^2).

itation over monsoonal Asia is up to 3 mm/day higher during Pmin in EC-Earth, up to 2 mm/day higher in GFDL and up to 2.5 mm/day higher in CESM. Furthermore, in line with the insolation forcing, the seasonality is greater in Pmin. The largest precipitation changes occur over the Himalaya, just south of the Tibetan plateau, see Figure 3. Models are also consistent in producing more precipitation during Pmin over most of the South-East Asian Peninsula, Indonesia and the western Indian Ocean. Reduced precipitation occurs over the eastern Indian Ocean, Bay of Bengal and the Chinese Seas. East of the Tibetan Plateau CESM simulates reduced precipitation as well, whereas EC-Earth shows slightly more precipitation, as does GFDL. This could be related to CESM having much more precipitation in the Pmax experiment in this area than the other models (contours in Figure 3). Models differ over India as well, with CESM and EC-Earth for instance showing high precipitation just west of the Western Ghats during Pmax, and lower precipitation during Pmin. This could be related to representation of orography (Figure B.1).

To assess the precipitation changes in more detail, we first investigate changes in surface temperature, surface pressure and surface winds. The hydrological cycle and upper level circulation features will be discussed in later paragraphs.

For precession, higher summer insolation results in higher surface air temperatures (Figure 4), except for monsoonal North-Africa / westernmost Arabian Peninsula and northwest India / Pakistan. Strong increases in cloud cover over these areas (not shown) decrease the amount of solar radiation reaching the surface. In addition, increased evaporation cools the surface. These monsoon-intensification feedbacks thus completely overcome the direct warming effect of increased insolation. In CESM these feedbacks seem particularly strong, resulting in a stronger cooling over a larger area of India and Pakistan than in EC-Earth and GFDL (Figure C.1). The rest of the continent warms up strongly, more than 8°C over continental Asia and 10°C over the Middle East. Warming over the ocean is smaller due to its large heat capacity. Over south-east Asia, the temperature response over land (south of $\sim$25°N) is dampened by a small

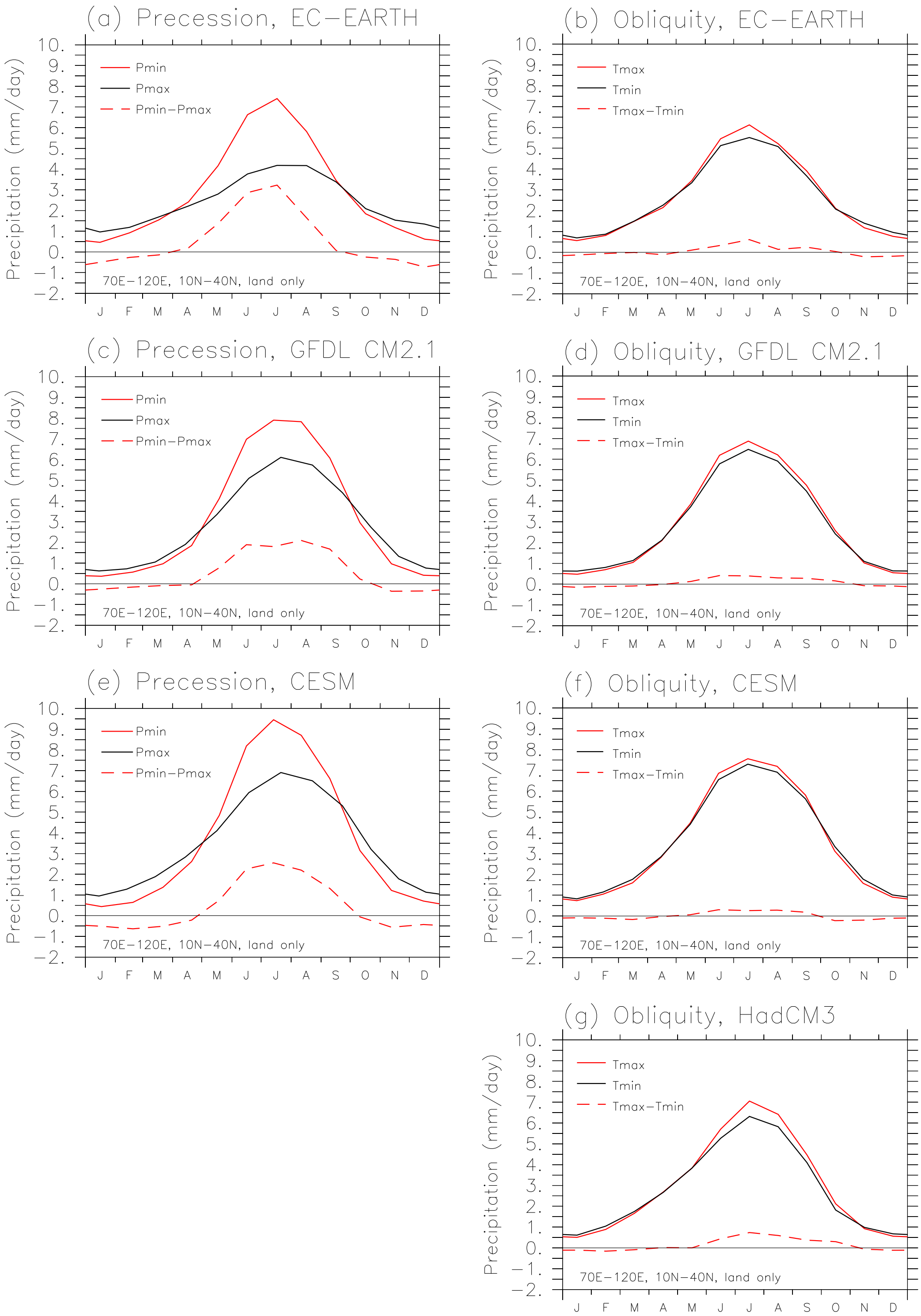

Figure 2: Precipitation over Asia per model, in mm/day, averaged over 70°E:120°E, 10°N:40°N land only for precession (a,c,e) and obliquity (b,d,f,g). Differences are given by the dashed lines.

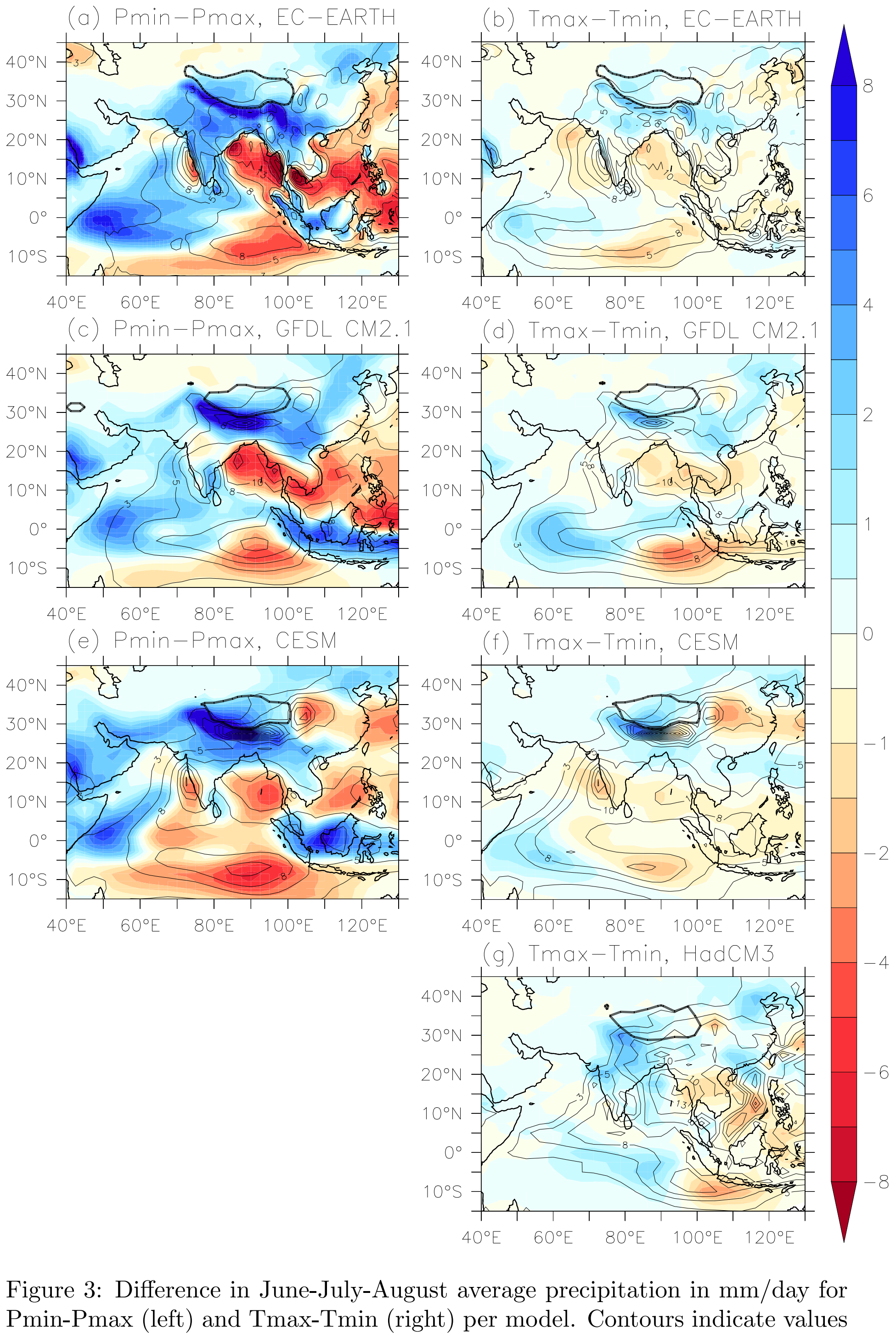

Figure 3: Difference in June-July-August average precipitation in mm/day for Pmin-Pmax (left) and Tmax-Tmin (right) per model. Contours indicate values for Pmax (left; a, c, e) or Tmin (right; b, d, f, g). The thick contour line is at 4km height, indicating the Tibetan Plateau.

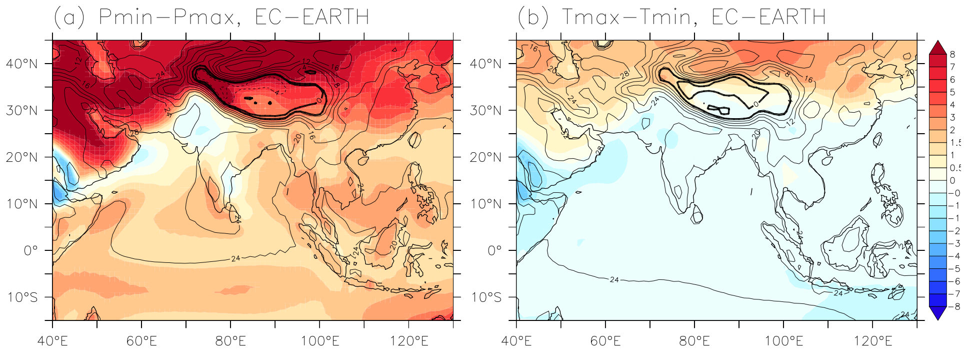

Figure 4: June-July-August average surface air temperature difference for Pmin-Pmax (left) and Tmax-Tmin (right) for EC-Earth. Results for all models can be found in the Supplementary Materials (Figure C.1). Contours indicate values for Pmax (left) or Tmin (right) in °C. The thick contour line is at 4km height, indicating the Tibetan Plateau.

increase in cloud cover and increased evaporative cooling.

In response to increased summer temperatures over the continent, sea level pressure over these regions is reduced (Figure 5), mostly over continental Asia and the Middle East. Over the Tibetan Plateau, southern India, the Bay of Bengal, South-East Asia and the Chinese Seas, sea level pressure is higher during Pmin in EC-Earth. The area of higher surface pressure over South-East Asia is connected to a strengthened North Pacific High (Figure 5) in all models (Figures C.2, C.3). CESM displays a stronger pressure increase over southern and south-east Asia as well as over the Indian Ocean compared to EC-Earth and GFDL (Figure C.3).

The strengthened North Pacific High and the lower surface pressure over central and eastern Asia force stronger southerly moisture transport over the EASM (Figure 5), related to stronger southerly winds (Figure 7). Over the northern Indian Ocean, the high pressure anomaly pushes winds and moisture transport more westward and reduces windspeed through a weaker meridional pressure gradient between the equator and ∼10-15°N. Just south of the equator the meridional pressure gradient is stronger and winds as well as moisture transport are stronger (Figures 5, 7). Monsoonal winds and moisture transport over the northernmost Arabian Sea and Bay of Bengal are stronger as well. Wind and moisture transport changes in GFDL and CESM are very similar, except over the northernmost Arabian Sea / south-eastern Arabian peninsula (Figures C.7, C.2, C.3).

To investigate the source of the increased monsoon precipitation during Pmin, we also considered evaporation. Figure 8 shows that evaporation over land is increased in most areas. This increase, up to 3 mm/day, is small compared to the precipitation increase, which reaches 15 mm/day in EC-Earth (Figure 3). Precipitation is redistributed with less precipitation over the surrounding oceans (except the western tropical Indian Ocean) and more over land during Pmin (Figure 3). There is no additional moisture source from ocean evaporation over the northern Indian Ocean (Figure 8), where evaporation is reduced in relation to reduced wind speed (Figure 7). Just south of the equator evaporation and wind speed are higher during Pmin, so this southern hemisphere region can act as a source of enhanced precipitation over the western Indian Ocean as well as the northern hemisphere (NH) Asian continent. Furthermore, looking at a larger area reveals enhanced moisture transport from the western tropical Pacific into the Indian Ocean. As a result of enhanced surface pressure over both the North and South Pacific (Figure 5), westwards wind and moisture transport (Figures 7 and 5) is strengthened at tropical latitudes, extending westward moisture transport into the western Indian Ocean. Over the western tropical Pacific, this results in lower net precipitation (Figure 5). The surface latent heat flux over regions of enhanced evaporation (southern hemisphere tropical Indian Ocean, western tropical Pacific) is enhanced, following the same patterns as evaporation, Figure 8. GFDL and CESM also show an overall increase of evaporation over land as well as the southern Indian Ocean (Figure C.8), and furthermore also display enhanced wind and moisture transport from the western tropical Pacific into the Indian Ocean (Figures C.2, C.3).

The enhanced precipitation and moisture transport into the ISM area despite lower evaporation over the northern Indian Ocean, can thus be related

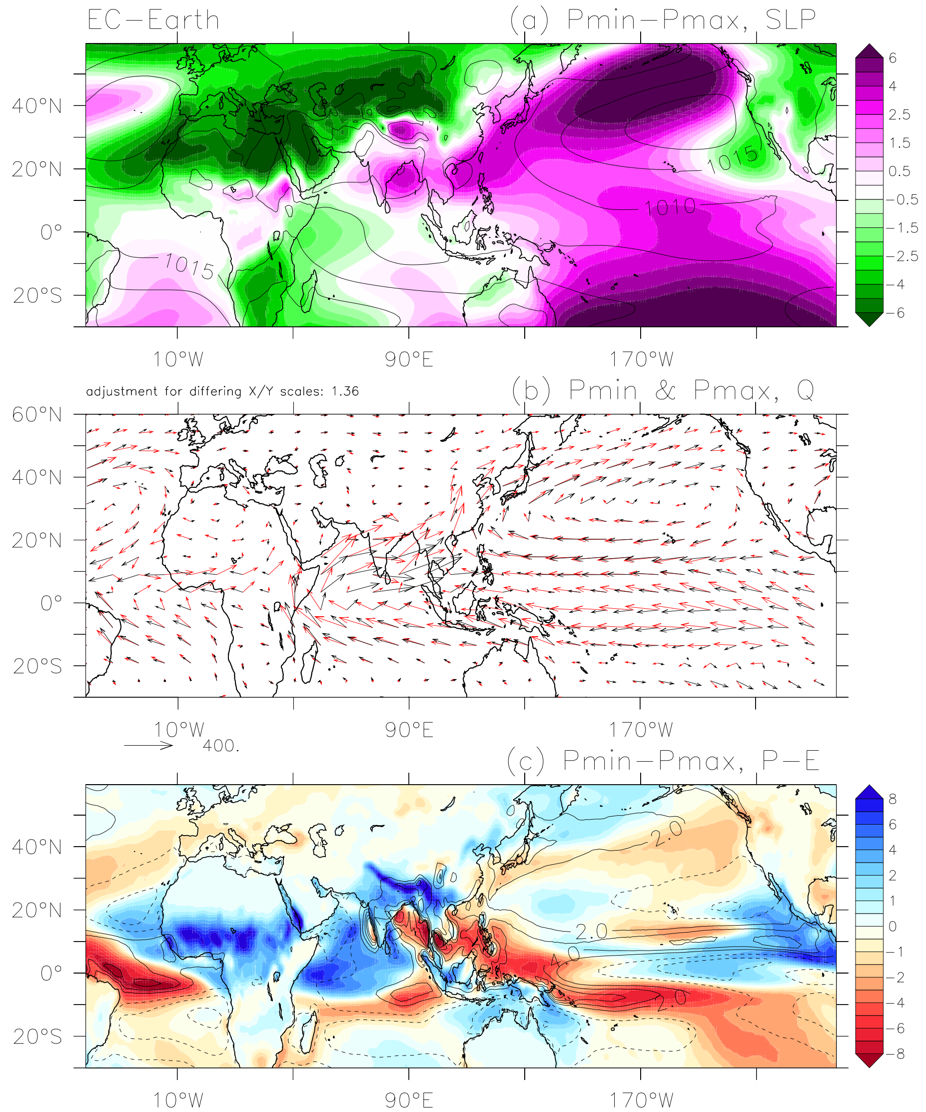

Figure 5: June-July-August average results for EC-Earth Pmin-Pmax. Top (a) shows sea level pressure difference in hPa with Pmax values in contours. Middle (b) shows moisture transport **Q**, the vertical integral of q**v** in kg/(ms), during Pmin in red, and Pmax in black. Daily q and **v** output from EC-Earth was used to compute **Q**. Bottom (c) shows net precipitation with positive values (blue) indicating increased net precipitation in mm/day and contours showing net precipitation during Pmax JJA. Results for all models can be found in the Supplementary Materials (Figure C.2 and C.3).

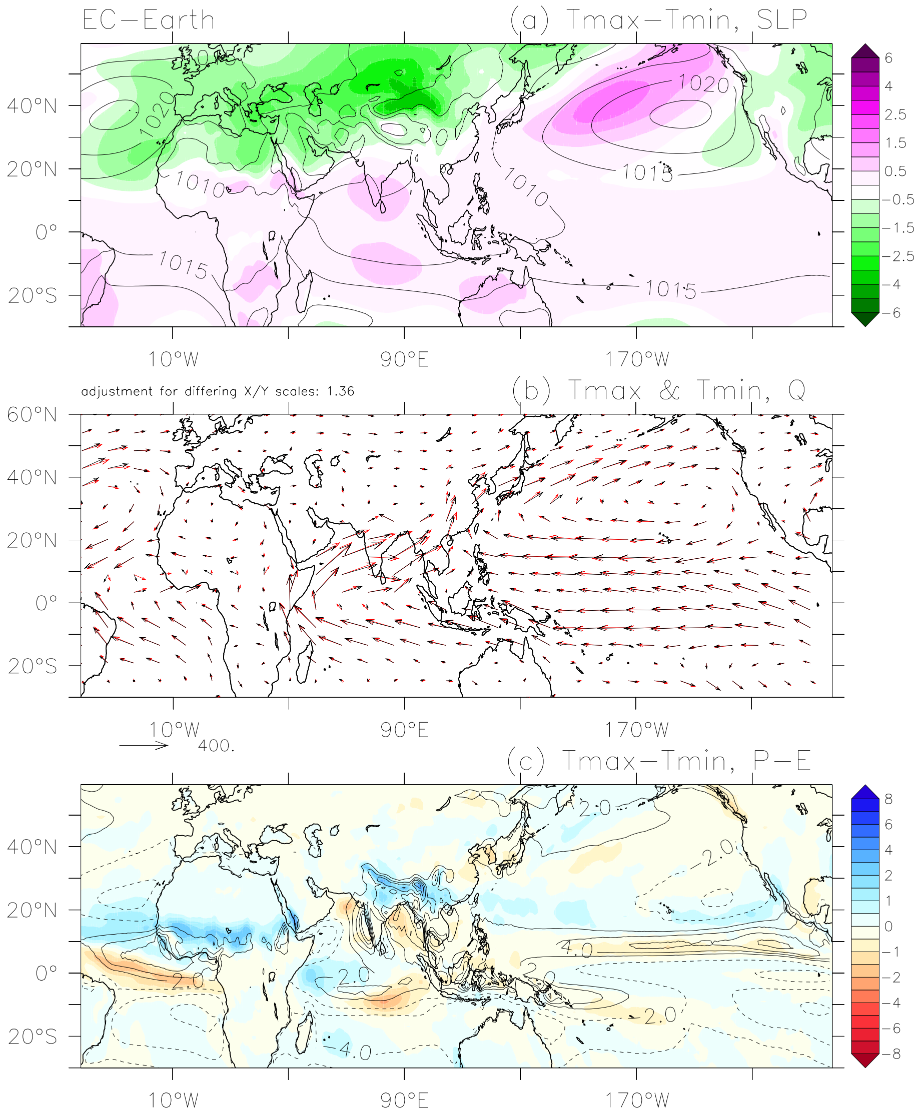

Figure 6: June-July-August average results for EC-Earth Tmax-Tmin. Top (a) shows sea level pressure difference in hPa with Tmin values in contours. Middle (b) shows moisture transport **Q**, the vertical integral of q**v** in kg/(ms), during Tmax in red, and Tmin in black. Daily q and **v** output from EC-Earth was used to compute **Q**. Bottom (c) shows net precipitation with positive values (blue) indicating increased net precipitation in mm/day and contours showing net precipitation during Tmin JJA. Results for all models can be found in the Supplementary Materials (Figures C.4, C.5, C.6).

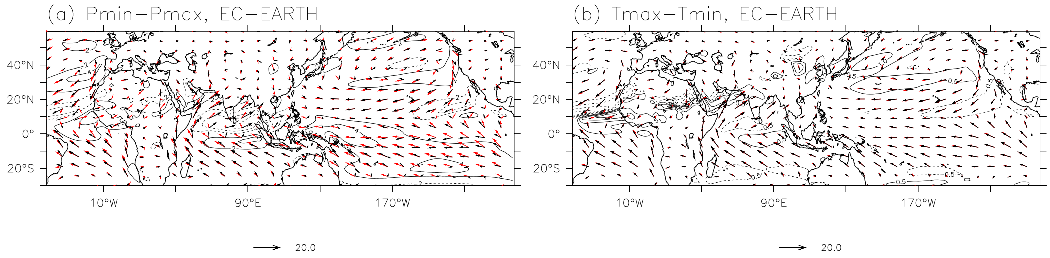

Figure 7: June-July-August average surface wind in m/s during Pmin (red) and Pmax (black, left), Tmax (green) and Tmin (blue, right) in EC-Earth. Contours indicate windspeed differences. Positive values are given by solid lines, negative values by dashed lines. The contour intverval for precession (left) is 2 m/s and 0.5 m/s for obliquity (right). Results for all models can be found in the Supplementary Materials (Figure C.7).

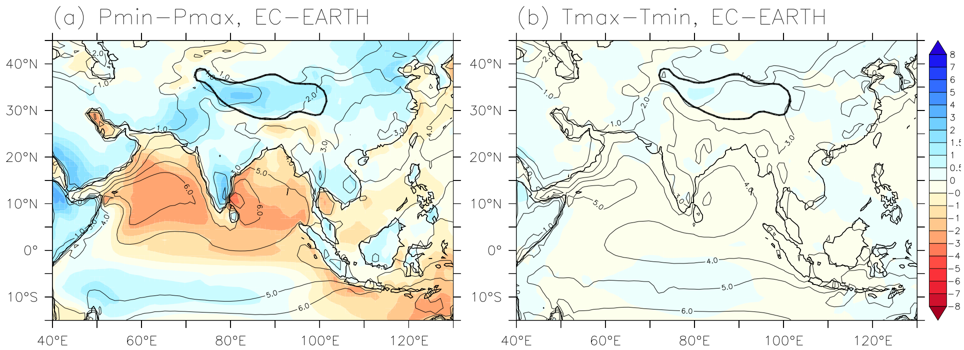

Figure 8: June-July-August average evaporation difference in mm/day for Pmin-Pmax (left) and Tmax-Tmin (right) for EC-Earth. Positive values (blue) indicate increased evaporation. Results for all models can be found in the Supplementary Materials (Figure C.8). Contours indicate values for Pmax (left) or Tmin (right). The thick contour line is at 4km height, indicating the Tibetan Plateau.

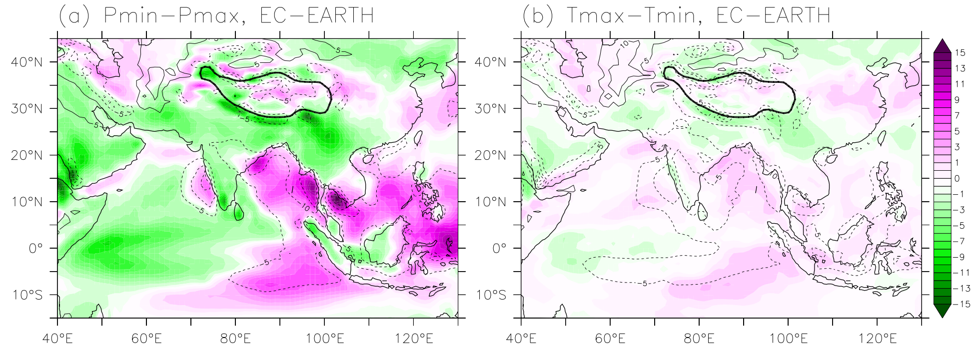

Figure 9: June-July-August average vertical velocity at 500 hPa in 10^{-2} Pa/s difference for Pmin-Pmax (left) and Tmax-Tmin (right). Contours indicate values for Pmax (left) or Tmin (right) with negative values indicating upward motion. Green indicates more upward or less downward motion, purple indicates more downward or less upward motion. Results for all models can be found in the Supplementary Materials (Figure C.13). The thick contour line is at 4km height, indicating the Tibetan Plateau.

to enhanced moisture transport from the southern Indian Ocean as well as the western tropical Pacific Ocean. Both the enhanced westward wind and moisture transport from the Pacific, as well as the reduced wind speeds over the northern Indian Ocean causing lower evaporation, are associated with anomalously high pressure. Increased specific humidity (not shown) over the northern Arabian Sea and East Asia plays a small role, but the major factor in the moisture transport changes is wind (compare Figure 7 and 5). A breakdown of moisture transport confirms the major role of wind in precession-induced moisture transport changes (see Supplementary Figure C.9). In CESM and GFDL the dynamic (wind-driven) part of moisture transport changes is strongest as well (Figures C.10, C.11). See Equation 1 in Bosmans et al. (2015a) for the breakdown of moisture transport into wind- and / or humidity-driven parts.

Changes in the middle troposphere are consistent with the surface precipitation changes. Figure 9 shows stronger convection (upward motion) along the Himalayas during Pmin, as well as stronger convection over the rest of monsoonal Asia and the western Indian Ocean. Over the ocean regions where precipitation is lower, convection is reduced. The same holds for GFDL and CESM (Figure C.13).

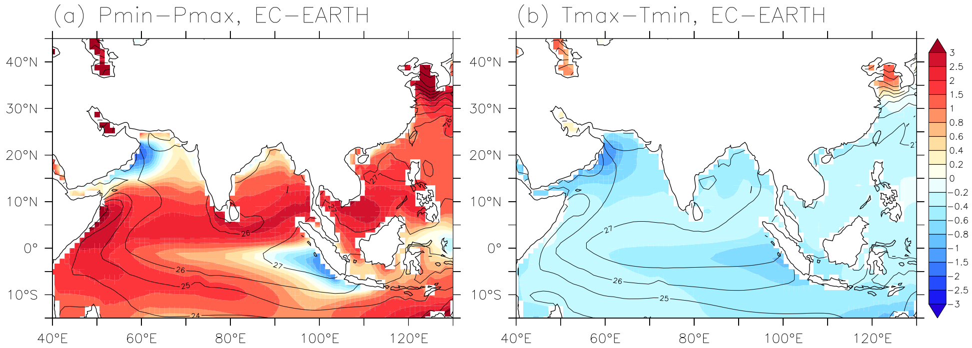

Figure 10: June-July-August average sea surface temperature in °C difference for Pmin-Pmax (left) and Tmax-Tmin (right). Contours indicate values for Pmax (left) or Tmin (right). Results for all models can be found in the Supplementary Materials (Figure C.14).

The increased precipitation, reduced surface pressure and increased convection over the western Indian Ocean during Pmin are characteristic of a positive Indian Ocean Dipole (IOD) pattern (Saji et al., 1999). Surface winds along the equator are more westward (Figure 7), conceivably forced westward by the high surface pressure anomaly over south-eastern Asia (Figure 5). Because of the more westward winds, there is more upwelling in the east near Sumatra, and warm waters reach further west, reducing the east-west sea surface temperature gradient over the tropical Indian Ocean (Figure 10). Warmer sea surface temperatures in the western Indian Ocean reduce surface pressure and support increased convection. Furthermore, cooler sea surface temperatures in the north-western Arabian Sea, at the coast of Oman, are indicative of more upwelling due to stronger north-eastward monsoon winds during Pmin. Similar sea surface temperature changes are produced by GFDL and CESM (Figure C.14), with particularly strong cooling west of Sumatra in CESM which could be related to relatively strong east-west sea level pressure difference in CESM as well as a strong increase in westward winds (however, note that the wind for CESM is plotted at the lowest pressure level, roughly 66m above the surface instead of at 10m as for the other models, Figure C.7).

3.2 Obliquity

Obliquity-induced insolation changes are smaller than precession-induced changes, in line with the insolation forcing. The JJA averaged insolation between 10°N and 40°N is ∼6 Wm^{-2} higher during Tmax than Tmin. At the same time SH insolation is reduced, creating an increased interhemispheric insolation gradient (Figure 1) (Bosmans et al., 2015b).

Summer precipitation is slightly higher during Tmax over monsoonal Asia, on the order of 0.5 mm/day (Figure 2). Precipitation patterns during Tmax and Tmin are quite similar, but during Tmax precipitation is increased just south of the Tibetan plateau, parts of south-eastern Asia and over the western Indian Ocean. There is inter-model spread in the pattern of change, which can at least partly be explained by differences in the control experiment (Tmin, contours in Figure 3 on the right). For instance, the precipitation maxima over the eastern Indian Ocean is located in different locations, but all models show decreased precipitation during Tmax over these locations. CESM shows decreases in precipitation over eastern China and south-east of the Tibetan plateau, which could be related to CESM's high precipitation rates during Tmin in these areas.

Summer temperatures are higher north of 25-30°N during Tmax, because of the small heat capacity of the continent and the fact that the NH insolation increase is stronger towards the higher latitudes. Over India and South-East Asia temperatures are slightly lower because of increased cloud cover, especially over Pakistan and India in the NH (Figure 4). In the SH temperatures are lower due to decreased JJA insolation during Tmax. Some parts of the Indian Ocean do not show a cooling during Tmax in CESM and GFDL (Figure C.1).

Changes in surface pressure roughly follow the temperature changes over the continent and the Indian Ocean; surface pressure is lower over the continent north of ∼25°N and higher south of ∼25°N (Figure 6). As for Pmin, the North Pacific High is stronger during Tmax (Figure 6). Over southern India / the northern Indian Ocean pressure is also slightly increased in EC-Earth and CESM (Figure C.5). Related to the decreased meridional pressure gradient over this area, wind speeds are decreased and slightly more westward (Figure 7). Just south of the equator wind speeds are increased, especially west of Sumatra. Monsoon winds in the northern Arabian Sea, Bay of Bengal and Chinese Seas are increased, in line with stronger monsoons during Tmax. Stronger monsoon winds over East Asia are in agreement with a stronger east-west pressure gradient, as surface pressure is reduced over land and increased over the North Pacific (Figure 6). Similar patterns over the coasts of the monsoon areas emerge from all models (Figure C.7), with some model differences in wind speed changes over the Indian Ocean and the coasts of East Asia.

The stronger monsoon winds over the coasts bring more moisture into the continent; moisture transport over these regions is generally increased (Figure 6). Over the south-western tropical Indian Ocean moisture transport is slightly reduced, due to both weaker winds and reduced specific humidity (not shown). The latter is related to reduced JJA insolation and lower temperatures over the tropics and the SH during Tmax. This decrease in moisture transport as well as the increase over the coast of the ISM area is also displayed by HadCM3 and CESM, while GFDL shows slightly stronger moisture transport over the south-western tropical Indian Ocean (Figures C.4, C.5, C.6). Over the East Asian coasts, moisture transport into the EASM area is increased in all models, with some inter-model difference in the direction of change. Further model difference occurs in the moisture transport from the tropical Pacific Ocean, which does not occur in EC-Earth and CESM but does occur in GFDL and HadCM3. There does not seem to be a consistent difference in surface pressure changes over the tropical and southern Pacific ocean to accompany these inter-model differences in moisture transport.

Changes in evaporation over both land and sea are small (Figure 8). This supports our finding that the increased monsoonal precipitation during Tmax is not related to increased local recycling over land nor to enhanced nearby ocean evaporation, but to a redistribution of precipitation from ocean to land and changes in moisture transport. A small increase in evaporation and moisture transport occurs over the southern tropical Indian Ocean (Figures 8, 6), but not in HadCM3 (Figure C.8). The latter could be related to HadCM3 producing increased precipitation over the western Indian Ocean much further east than the other models (see for instance net precipitation in Figure C.6). The reduced moisture transport from the tropical Pacific is related to both changes in wind as well as specific humidity in EC-Earth (see Supplementary Figure C.9). The reduced moisture transport over this area in CESM is mostly related to wind (Figure C.11), as is the increased moisture transport displayed by GFDL and HadCM3 (Figures C.10, C.12). In the moisture transport over the coasts into the ISM and EASM area, wind changes play a major role in all models (see Supplementary Figure C.9 and C.10, C.11, C.12), with stronger southerly flow over the EASM and more westward flow over the Indian Ocean related to anomalously high pressure (Figure 6).

The vertical velocity at 500 hPa (Figure 9) further shows the redistribution of precipitation: upward velocity (convection) is reduced over the oceans and increased over land, mostly over the regions with the strongest precipitation increase (Figure 3). The exception to this land / ocean response is the western tropical Indian Ocean, where during Tmax convection is slightly stronger and precipitation is higher. This pattern of vertical velocity change, overlaying precipitation changes, can also be seen in all models (Figure C.13). The Indian Ocean Dipole (IOD)-like pattern is similar to the Pmin-Pmax anomalies described in Section 3.1, with more westward winds along the equator and a reduced east-west sea surface temperature gradient. Sea surface temperatures are overall lower during Tmax due to reduced JJA insolation over most of the tropics and SH in EC-Earth. A colder sea surface is also a reason for the lack of decreased surface pressure over the western Indian Ocean (Figure 6). Nonetheless the cooling effect of increased upwelling during Tmax can be seen in the east, near Sumatra, as well as over the north-western Arabian Sea, near the coast of Oman where winds are stronger (Figure 10, 7). These upwelling features can be seen in other models as well, despite differences in sea surface temperature change. CESM and GFDL show slightly warmer temperatures over parts of the Indian Ocean (Figure C.14).

4 Discussion

This is the first study to investigate the separate effects of precession and obliquity at high resolution using multiple GCMs. We have shown that monsoon precipitation is enhanced over Asia during minimum precession and maximum obliquity (Pmin and Tmax), when summer insolation in the Northern Hemisphere (NH) is increased. Here we discuss how our results compare to previous modelling studies, how the responses to precession and obliquity differ, and the possible implications for proxy climate studies of the Asian monsoons.

4.1 Previous model studies

Overall, the strengthening of the Asian monsoons at times of precession-induced increased NH summer insolation is recognized in many paleoclimate modelling studies. The mid-Holocene is often used for orbital studies and is a selected timeslice of the Paleoclimate Modelling Intercomparison Project (PMIP), when perihelion occurred in autumn and the insolation difference compared to present-day is similar to but of smaller amplitude than the Pmin-Pmax difference used here. In a Mid-Holocene study performed with EC-Earth, the same model version as used here, we therefore found similar but smaller changes compared to the precession-induced changes reported in this present study (Bosmans et al., 2012). These changes are consistent with other PMIP studies which overall report enhanced southerly monsoon winds over East Asia related to an enhanced land-sea thermal contrast and increased pressure over the Pacific as well as increased convection over land (Jiang et al., 2013; Tian and Jiang, 2013; Wang and Wang, 2013; Zheng et al., 2013; Sun et al., 2015). The increased surface pressure along south-east Asia and the Indian Ocean Dipole (IOD) pattern of increased precipitation over the western Indian Ocean are reported for the Mid-Holocene as well (Zhao et al., 2005; Jiang et al., 2013). There is however some model spread in location and magnitude of changes (Zhao et al., 2005; Wang and Wang, 2013). Abram et al. (2007) find stronger IOD events during the Mid-Holocene in model simulations as well as sea surface temperature and precipitation proxy records.

The few studies that also focus on idealized extreme precession forcing report enhanced monsoon precipitation over India and East Asia (Erb et al., 2013; Mantsis et al., 2013), but do not discuss the Asian monsoon in detail. However, Mantsis et al. (2013) as well as Wu et al. (2016) provide an explanation for the strengthened North Pacific High at times of enhanced summer insolation. This strengthening is forced locally through decreased latent heat release over the ocean and a more stable air column, as well as remotely through diabatic heating over monsoon areas where latent heat release is increased, in line with stronger monsoon precipitation. Wang et al. (2012) also identified a strengthened North Pacific High during minimum precession, related to tropospheric cooling which is suggested to be related reduced local latent heat release as well as to land surface heating. Higher surface pressure over the North Pacific is also modeled by Shi et al. (2011). Moreover, Mantsis et al. (2013) display an IOD pattern in their precipitation anomalies over the tropical Indian Ocean (Figure 3), as do time slices with minimum precession in Wang et al. (2012), Battisti et al. (2014) Rachmayani et al. (2016) and Erb et al. (2015), the latter using the same GFDL model output used here. Wang et al. (2012) furthermore show enhanced westward moisture transport from the tropical Pacific, and Battisti et al. (2014) show enhanced westward winds.

In idealized experiments of high (maximum) and low (minimum) obliquity using the same GFDL model output used here, Erb et al. (2013) display weakened NH monsoons over northern Africa, India, and parts of China during low obliquity. Chen et al. (2011b) also investigate the effect of obliquity on the Asian monsoons, reporting increased summer precipitation over India and south-east

Asia during high obliquity. They further suggest a dipole pattern over eastern Asia, with decreased north-east Asian precipitation during high obliquity. Although we see a small area of precipitation decrease over north-east Asia during Tmax as well, this "dipole" is not as strong as in Chen et al. (2011b) except for CESM. Furthermore, they do not observe enhanced precipitation over the western Indian Ocean and show a different surface pressure and wind anomaly pattern compared to our obliquity results. These differences may be due to model and / or resolution differences; their study uses a coarse resolution of $\sim$7.5°x4°. The obliquity experiments of Tuenter et al. (2003) do not show an IOD-like pattern either, which may also be related to coarse resolution and / or to model shortcomings (Bosmans et al., 2015a). Rachmayani et al. (2016) show a drier northern EASM as in CESM and Chen et al. (2011b), but show drying over most of India and no increased precipitation over the western Indian Ocean unlike most of the obliquity results shown here.

Although our model results are in line with other model experiments for precession-induced monsoon changes, there is a larger inter-model spread in the obliquity-induced monsoon changes, within the models presented here as well as compared to literature. This could at least partly be related to the much weaker insolation forcing associated with obliquity, whereas the large precession-induced forcing results in much more similar responses. The addition of components that are lacking from our models may result in slightly different responses. Our simulations do not include a dynamic vegetation module. Changing vegetation patterns can have a small effect on the monsoonal response to orbital forcing (e.g. Dallmeyer et al., 2010; Tian and Jiang, 2013). Furthermore, dynamic ice sheets are not included and therefore changes in ice sheet volume or area do not play a role in the monsoonal response discussed here. Our findings imply that the ISM and EASM can respond directly to (sub-)tropical insolation changes. A more detailed discussion on how obliquity influences low-latitude climate without a high-latitude influence can be found in Bosmans et al. (2015b).

4.2 Precession vs. obliquity

The precession-induced changes in insolation are different from those induced by obliquity (Tuenter et al., 2003; Bosmans et al., 2015a). During NH summer (JJA), insolation is increased in the northern hemisphere during both Pmin and Tmax, while at the same time in the SH insolation is also increased during Pmin but decreased during Tmax. At first glance the Asian monsoon changes seem very similar, albeit weaker for obliquity. For both a strengthening of the North Pacific High occurs, creating an increased land/sea pressure gradient over East Asia, resulting in stronger northward monsoon winds. There is increased surface pressure over south-eastern Asia, decreased windspeeds over the northern Indian Ocean and increased precipitation over the tropical western Indian Ocean for both precession and obliquity. Over the southern Pacific Ocean, pressure is increased during Pmin but not during Tmax, which may explain why westward winds and moisture transport are enhanced during Pmin but not during Tmax. There is however disagreement amongst the models in the direction of change in wind and moisture transport from the Pacific. Changes in sea surface temperature are different between precession and obliquity, due to the JJA SH increase in insolation during Pmin and decrease during Tmax. This results in overall warmer sea surface temperatures during Pmin and colder temperatures during Tmax, the latter being the likely cause of the lack of lower surface pressure over the western tropical Indian Ocean during Tmax. We note however that there is some inter-model spread in the obliquity response of Indian Ocean SSTs. Also, lower temperatures result in lower specific humidity and lower moisture transport over the the western Indian Ocean, which were increased for Pmin related to higher JJA insolation and temperatures.

4.3 Proxy climate record studies

Our experiments suggest that the ISM and EASM may respond instantaneously to orbital forcing. Comparing our snapshot experiments of orbital extremes directly to transient proxy climate records in terms of phasing is admittedly not straightforward, and we cannot claim that an instantaneous response is always the case since we did not perform transient simulations nor included other boundary conditions such as glacial cycles. However, a direct response of (Asian) monsoons to summer insolation on the orbital time scales is noticed in several studies. Model studies performing transient simulations over multiple orbital cycles find that June-July-August precipitation is in phase with average June insolation (Kutzbach et al., 2008) or June 21^{st} insolation (Weber and Tuenter, 2011). The latter study further shows that for precession the monsoon remains in phase even when ice sheets are included. Recent speleothem oxygen isotope records from South and East Asia (e.g. Wang et al., 2008; Cai et al., 2015; Kathayat et al., 2016), spanning multiple glacial cycles, show no significant lag between the ISM and the EASM and northern hemisphere summer insolation at the precession band. Yet a small offset between models and proxy records remains, with speleothem oxygen isotope records typically in phase with July or July 21^{st} insolation, while model studies suggest that monsoonal precipitation is in phase with June or June 21^{st} insolation,

Nevertheless both types of study suggest a much shorter phase lag with respect to precession than previously suggested by e.g. Clemens and Prell (2003); Caley et al. (2011) (for an overview see Liu and Shi (2009); Battisti et al. (2014); Wang et al. (2014, 2017)). Lags of up to 9 kyr for precession and 6 kyr for obliquity are derived from marine productivity proxies under the assumption that productivity is directly related to monsoon wind strength and upwelling. Thus our results suggest that productivity may be related to other processes (see also Ziegler et al. (2010)). Le Mézo et al. (2016) have recently shown that productivity is not necessarily enhanced at times of a stronger ISM during the last glacial-interglacial cycle. Furthermore, we find that not only upwelling over the western Arabian Sea but also evaporation and latent heat release from the southern tropical Indian Ocean can respond instantaneously to increased northern hemisphere insolation. Therefore, we do not agree with the pronounced lag and mechanisms of the ISM in the precession band in the late Pleistocene proposed by e.g. Clemens and Prell (2003) and Caley et al. (2011), who claim that latent heat export from the southern hemisphere into the ISM region is maximized during Pmax, when SH summer insolation is high (Ruddiman, 2006a). According to these mechanisms, the ISM should be stronger during Pmax. The recent speleothem records mentioned above also disagree with this mechanism, with Kathayat et al. (2016) stating that their results do not suggest a dominant influence on the ISM of southern hemisphere climate processes. We do note, however, that the discussion on interpreting cave oxygen isotope records is ongoing (Caley et al., 2014; Mohtadi et al., 2016; Wang et al., 2017).

Further investigation into a possible lag in the response time of the Asian monsoons to orbital forcing is necessary. An alternative explanation for the discrepancy in model studies which do not find lags and the range of lags found in proxy records is that monsoons may respond more strongly to a phase of precession other than maximum or minimum precession (e.g. Marzin and Braconnot, 2009; Erb et al., 2015). For example, if the strongest monsoons are produced when perihelion occurs sometime after the summer solstice, this will appear as a lag with respect to the precession parameter in the proxy record even if the climate system is directly responding to the imposed forcing (see e.g. Figure 3 in Erb et al. (2015)). Another aspect that may appear as a lag in the monsoon strength relative to insolation is the interruption by cold spells such as the Younger Dryas or meltwater spikes in the North Atlantic affecting meridional overturning (e.g. Wang et al., 2008; Ziegler et al., 2010; Mohtadi et al., 2016; Cheng et al., 2016). Such events could cause a longer, up to 3 kyr, lag during major deglaciation. Like ice sheet variations these aspects are not included in this model study. Additional time slice or transient experiments, including ice sheets and potentially Atlantic meltwater fluxes, could shed more light on this discussion.

5 Conclusion

This study set out to investigate the effects of both precession and obliquity on the Asian summer monsoons, using four fully coupled general circulation models; EC-Earth, GFDL, CESM and HadCM3. We demonstrate the effect of both precession and obliquity on the Asian summer monsoons, with increased monsoon precipitation and convection over the continent during minimum precession and maximum obliquity related to wind-driven changes in moisture transport. Over East Asia the southerly monsoon flow and moisture transport is strengthened by an intensified North Pacific High and the subsequent increase in the land/sea pressure gradient. Over the Indian monsoon region changes are less straightforward. Anomalously high pressure over south-east Asia weakens the monsoon winds over most of the northern Indian Ocean, reducing evaporation. Over the tropical Indian Ocean an Indian Ocean Dipole pattern emerges with enhanced precipitation over the western Indian Ocean. Therefore these effects damp the enhanced landward moisture transport and monsoonal precipitation over the continent. The influence of obliquity is smaller than that of precession, and shows a different response in temperature and humidity over the Indian Ocean due to reduced insolation over the southern hemisphere. However, for both precession and obliquity wind speed and evaporation is increased over the southern Indian Ocean. For precession, the western tropical Pacific acts as a moisture source as well. Wind speed, and therefore also upwelling, is increased near the coast of Oman. Our results thus show that a direct response to precession and obliquity forcing is possible, in line with speleothem records but in contrast to marine proxy climate records, which suggest a significantly longer lag in response.

Acknowledgments

The EC-Earth experiments were performed by Joyce Bosmans, who was funded by a "Focus en Massa" grant of Utrecht University, the Netherlands. Computing time for EC-Earth was provided by the Royal Netherlands Meteorological Institute (KNMI) and the European Center for Medium-range Weather Forecast (ECMWF). Michael Erb performed the GFDL CM2.1 and CESM experiments, and was supported by a postdoctoral fellowship from the University of Texas Institute for Geophysics and a Paleo Perspectives on Climate Change grant from the National Science Foundation (Grant ATM0902735). Computing resources for GFDL CM2.1 were provided by the Geophysical Fluid Dynamics Laboratory at Princeton and resources for CESM were provided by the Climate Simulation Laboratory at NCAR's Computational and Informational Systems Laboratory (ark:/85065/d7wd3xhc), which is sponsored by the National Science Foundation and other agencies. We would like to thank Tony Broccoli for help running the GFDL CM2.1 experiments and Charles Jackson for guidance in running CESM. The Had-CM3 experiments were performed by Aisling Dolan, James Pope and Dominic Edge. Aisling Dolan acknowledges receipt of funding from the European Research Council under the European Union's Seventh Framework Programme (FP7/2007-2013)/ERC grant agreement no. 278636 and also the EPSRC-funded Past Earth Network.

References

Abram, N. J., Gagan, M. K., Liu, Z., Hantoro, W. S., McCulloch, M. T., and Suwargadi, B. W.: Seasonal characteristics of the Indian Ocean Dipole during the Holocene epoch, Nature, 445, 299–302, 2007.

Araya-Melo, P. A., Crucifix, M., and Bounceur, N.: Global sensitivity analysis of the Indian monsoon during the Pleistocene, Climate of the Past, 11, 45–61, 2015.

Battisti, D., Ding, Q., and Roe, G.: Coherent pan-Asian climatic and isotopic response to orbital forcing of tropical insolation, Journal of Geophysical Research: Atmospheres, 119, 2014.

Berger, A. L.: Long-Term Variations of Daily Insolation and Quaternary Climatic Changes, Journal of the Atmospheric Sciences, 35, 2362–2367, 1978.

Bordoni, S. and Schneider, T.: Monsoons as eddy-mediated regime transitions of the tropical overturning circulation, Nature Geoscience, 1, 515, 2008.

Bosmans, J., Drijfhout, S., Tuenter, E., Hilgen, F., and Lourens, L.: Response of the North African summer monsoon to precession and obliquity forcings in the EC-Earth GCM, Climate Dynamics, 44, 279–297, 2015a.

Bosmans, J., Hilgen, F., Tuenter, E., and Lourens, L.: Obliquity forcing of low-latitude climate, Climate of the Past, 11, 1335–1346, 2015b.

Bosmans, J. H. C., Drijfhout, S. S., Tuenter, E., Lourens, L. J., Hilgen, F. J., and Weber, S. L.: Monsoonal response to mid-holocene orbital forcing in a high resolution GCM, Climate Of The Past, 8, 723–740, doi: 10.5194/cp-8-723-2012, 2012.

Braconnot, P. and Marti, O.: Impact of precession on monsoon characteristics from coupled ocean atmosphere experiments: changes in Indian monsoon and Indian ocean climatology, Marine Geology, 201, 23–34, doi: 10.1016/S0025-3227(03)00206-8, 2003.

Braconnot, P., Otto-Bliesner, B., Harrison, S., Joussaume, S., Peterchmitt, J. Y., Abe-ouchi, A., Crucifix, M., Driesschaert, E., Fichefet, T., Hewitt, C. D., Kageyama, M., Kitoh, A., Laine, A., Loutre, M. F., Marti, O., Merkel, U., Ramstein, G., Valdes, P., Weber, S. L., Yu, Y., and Zhao, Y.: Results of PMIP2 coupled simulations of the Mid-Holocene and Last Glacial Maximum – Part 1: experiments and large-scale features, Climate Of The Past, 3, 261–277, 2007.

Braconnot, P., Marzin, C., Gregoire, L., Mosquet, E., and Marti, O.: Monsoon response to changes in Earth's orbital parameters: comparisons between simulations of the Eemian and of the Holocene, Climate Of The Past, 4, 281–294, 2008.

Cai, Y., Fung, I. Y., Edwards, R. L., An, Z., Cheng, H., Lee, J.-E., Tan, L., Shen, C.-C., Wang, X., Day, J. A., et al.: Variability of stalagmite-inferred Indian monsoon precipitation over the past 252,000 y, Proceedings of the National Academy of Sciences, 112, 2954–2959, 2015.

Caley, T., Malaizé, B., Zaragosi, S., Rossignol, L., Bourget, J., Eynaud, F., Martinez, P., Giraudeau, J., Charlier, K., and Ellouz-Zimmermann, N.: New Arabian Sea records help decipher orbital timing of Indo-Asian monsoon, Earth and Planetary Science Letters, 308, 433 – 444, doi:http://dx.doi.org/10.1016/j.epsl.2011.06.019, URL http://www.sciencedirect.com/science/article/pii/S0012821X11003785, 2011.

Caley, T., Roche, D. M., and Renssen, H.: Orbital Asian summer monsoon dynamics revealed using an isotope-enabled global climate model, Nature communications, 5, 2014.

Cattle, H., Crossley, J., and Drewry, D.: Modelling arctic climate change, Philosophical Transactions of the Royal Society of London A: Mathematical, Physical and Engineering Sciences, 352, 201–213, 1995.

Chen, G.-S., Kutzbach, J., Gallimore, R., and Liu, Z.: Calendar effect on phase study in paleoclimate transient simulation with orbital forcing, Climate dynamics, 37, 1949–1960, 2011a.

Chen, G.-s., Zhengyu, L., Clemens, S. C., Prell, W. L., and Liu, X.: Modeling the time-dependent response of the Asian summer monsoon to obliquity forcing in a coupled GCM: a PHASEMAP sensitivity experiment, Climate Dynamics, 36, 695–710, doi:10.1007/s00382-010-0740-3, 2011b.

Cheng, H., Edwards, R. L., Sinha, A., Spötl, C., Yi, L., Chen, S., Kelly, M., Kathayat, G., Wang, X., Li, X., et al.: The Asian monsoon over the past 640,000 years and ice age terminations, Nature, 534, 640–646, 2016.

Clemens, S. C. and Prell, W. L.: A 350,000 year summer-monsoon multi-proxy stack from the Owen Ridge, Northern Arabian Sea, Marine Geology, 201, 35–51, 2003.

Dallmeyer, A., Claussen, M., and Otto, J.: Contribution of oceanic and vegetation feedbacks to Holocene climate change in monsoonal Asia, Climate Of The Past, 6, 195–218, 2010.

Delworth, T. L., Broccoli, A. J., Rosati, A., Stouffer, R. J., Balaji, V., Beesley, J. A., Cooke, W. F., Dixon, K. W., Dunne, J., Dunne, K., et al.: GFDL's CM2 global coupled climate models. Part I: Formulation and simulation characteristics, Journal of Climate, 19, 643–674, 2006.

Dolan, A. M., Haywood, A. M., Hill, D. J., Dowsett, H. J., Hunter, S. J., Lunt, D. J., and Pickering, S. J.: Sensitivity of Pliocene ice sheets to orbital forcing, Palaeogeography, Palaeoclimatology, Palaeoecology, 309, 98–110, 2011.

Erb, M. P., Broccoli, A. J., and Clement, A. C.: The contribution of radiative feedbacks to orbitally-driven climate change, Journal of Climate, doi:doi:10.1175/JCLI-D-12-00419.1, 2013.

Erb, M. P., Jackson, C. S., and Broccoli, A. J.: Using single-forcing GCM simulations to reconstruct and interpret Quaternary climate change, Journal of Climate, 28, 9746–9767, 2015.

Erb, M. P., Jackson, S., Broccoli, A. J., Lea, D. W., Valdes, P. J., Crucifix, M., and DiNezio, P. M.: Model evidence for a seasonal bias in Antarctic ice cores, in press, revisions submitted, 2018.

Gordon, C., Cooper, C., Senior, C. A., Banks, H., Gregory, J. M., Johns, T. C., Mitchell, J. F., and Wood, R. A.: The simulation of SST, sea ice extents and ocean heat transports in a version of the Hadley Centre coupled model without flux adjustments, Climate Dynamics, 16, 147–168, 2000.

Hazeleger, W., Severijns, C., Semmler, T., Stefanescu, S., Yang, S., Wyser, K., Wang, X., Dutra, E., Baldasano, J. M., Bintanja, R., Bougeault, P., Caballero, R., Ekman, A. M., Christensen, J. H., van den Hurk, B., Jimenez, P., Jones, C., Kallberg, P., Koenigk, T., McGrath, R., Miranda, P., van Noije, T., Palmer, T., Parodi, J. A., Schmith, T., Selten, F., Storelvmo, T., Sterl, A., Tapamo, H., Vancoppenolle, M., Viterbo, P., and Willen, U.: EC-Earth: A Seamless Earth System Prediction Approach in Action, Bulletin of the American Meteorological Society, 91, 1357–1363, 2010.

Hazeleger, W., Wang, X., Severijns, C., Stefanescu, S., Bintanja, R., Sterl, A., Wyser, K., Semmler, T., Yang, S., van den Hurk, B., van Noije, T., van der Linden, E., and van der Wiel, K.: EC-Earth V2.2: description and validation of a new seamless earth system prediction model, Climate Dynamics, doi: 10.1007/s00382-011-1228-5, 2011.

Jiang, D., Tian, Z., and Lang, X.: Mid-Holocene net precipitation changes over China: model–data comparison, Quaternary Science Reviews, 82, 104–120, 2013.

Kathayat, G., Cheng, H., Sinha, A., Spötl, C., Edwards, R. L., Zhang, H., Li, X., Yi, L., Ning, Y., Cai, Y., et al.: Indian monsoon variability on millennial-orbital timescales, Scientific reports, 6, 2016.

Kutzbach, J. E. and Guetter, P. J.: The Influence of Changing Orbital Parameters and Surface Boundary Conditions on Climate Simulations for the Past 18000 years, Journal of the Atmospheric Sciences, 43, 1726–1759, 1986.

Kutzbach, J. E. and Otto-Bliesner, B. L.: The Sensitivity of the African-Asian Monsoonal Climate to Orbital Parameter Changes for 9000 Years B.P. in a Low-Resolution General Circulation Model, Journal of the Atmospheric Sciences, 39, 1177–1188, 1982.

Kutzbach, J. E., Liu, X., Liu, Z., and Chen, G.: Simulation of the evolutionary response of global summer monsoons to orbital forcing over the past 280,000 years, Climate Dynamics, 30, 567–579, doi:10.1007/s00382-007-0308-z, 2008.

Le Mézo, P., Beaufort, L., Bopp, L., Braconnot, P., and Kageyama, M.: From Monsoon to marine productivity in the Arabian Sea: insights from glacial and interglacial climates, Climate of the Past Discussion, doi:10.5194/cp-2016-88, 2016.

Liu, X. and Shi, Z.: Effect of precession on the Asian summer monsoon evolution: A systematic review, Chinese Science Bulletin, 54, 3720–3730, 2009.

Mantsis, D. F., Clement, B., Kirtman, B., Broccoli, A. J., and Erb, M. P.: Precessional cycles and their influence on the North Pacific and North Atlantic summer anticyclones, Journal of Climate, doi:10.1175/JCLI-D-12-00343.1, 2013.

Marzin, C. and Braconnot, P.: Variations of Indian and African monsoons induced by insolation changes at 6 and 9.5 kyr BP, Climate Dynamics, 33, 215–231, doi:10.1007/s00382-009-0538-3, 2009.

Marzocchi, A., Lunt, D., Flecker, R., Bradshaw, C., Farnsworth, A., and Hilgen, F.: Orbital control on late Miocene climate and the North African monsoon: insight from an ensemble of sub-precessional simulations, Climate of the Past, 11, 1271–1295, 2015.

Mohtadi, M., Prange, M., and Steinke, S.: Palaeoclimatic insights into forcing and response of monsoon rainfall, Nature, 533, 191–199, 2016.

Molnar, P., Boos, W. R., and Battisti, D. S.: Orographic controls on climate and paleoclimate of Asia: thermal and mechanical roles for the Tibetan Plateau, Annual Review of Earth and Planetary Sciences, 38, 2010.

Pollard, D. and Reusch, D. B.: A calendar conversion method for monthly mean paleoclimate model output with orbital forcing, Journal of Geophysical Research: Atmospheres, 107, 2002.

Prell, W. L. and Kutzbach, J. E.: Monsoon Variability Over the Past 150,000 Years, Journal of Geophysical Research, 92, 8411–8425, 1987.

Prescott, C. L., Haywood, A. M., Dolan, A. M., Hunter, S. J., Pope, J. O., and Pickering, S. J.: Assessing orbitally-forced interglacial climate variability during the mid-Pliocene Warm Period, Earth and Planetary Science Letters, 400, 261–271, 2014.

Rachmayani, R., Prange, M., and Schulz, M.: Intra-interglacial climate variability: model simulations of Marine Isotope Stages 1, 5, 11, 13, and 15, Climate of the Past, 12, 677–695, doi:10.5194/cp-12-677-2016, URL http://www.clim-past.net/12/677/2016/, 2016.

Ruddiman, W. F.: What is the timing of orbital-scale monsoon changes?, Quaternary Science Reviews, 25, 657–658, 2006a.

Ruddiman, W. F.: Orbital changes and climate, Quaternary Science Reviews, 25, 3092–3112, 2006b.

Saji, N., Goswami, B. N., Vinayachandran, P., and Yamagata, T.: A dipole mode in the tropical Indian Ocean, Nature, 401, 360–363, 1999.

Shi, Z., Liu, X., Sun, Y., An, Z., Liu, Z., and Kutzbach, J.: Distinct responses of East Asian summer and winter monsoons to astronomical forcing, Climate of the Past, 7, 1363–1370, 2011.

Singarayer, J. S. and Valdes, P. J.: High-latitude climate sensitivity to ice-sheet forcing over the last 120kyr, Quaternary Science Reviews, 29, 43–55, 2010.

Sun, Y., Kutzbach, J., An, Z., Clemens, S., Liu, Z., Liu, W., Liu, X., Shi, Z., Zheng, W., Liang, L., et al.: Astronomical and glacial forcing of East Asian summer monsoon variability, Quaternary Science Reviews, 115, 132–142, 2015.

Tian, Z. and Jiang, D.: Mid-Holocene ocean and vegetation feedbacks over East Asia, Climate of the Past, 9, 2153–2171, doi:10.5194/cp-9-2153-2013, URL http://www.clim-past.net/9/2153/2013/, 2013.

Tuenter, E., Weber, S. L., Hilgen, F. J., and Lourens, L. J.: The response of the African summer monsoon to remote and local forcing due to precession and obliquity, Global and Planetary Change, 36, 219 – 235, doi:10.1016/S0921-8181(02)00196-0, 2003.

Valcke, S. and Morel, T.: OASIS3 user guide, Tech. rep., CERFACS, prism Technical Report, 68pp, available online at http://www.prism.enes.org/Publications/Reports/oasis3_UserGuide_T3.pdf, 2006.

Wang, P., Wang, B., Cheng, H., Fasullo, J., Guo, Z., Kiefer, T., and Liu, Z.: The Global Monsoon across Time Scales: coherent variability of regional monsoons, Climate of the Past, 10, 1–46, 2014.

Wang, P. X., Wang, B., Cheng, H., Fasullo, J., Guo, Z., Kiefer, T., and Liu, Z.: The global monsoon across time scales: Mechanisms and outstanding issues, Earth-Science Reviews, 174, 84–121, 2017.

Wang, T. and Wang, H.: Mid-Holocene Asian summer climate and its responses to cold ocean surface simulated in the PMIP2 OAGCMs experiments, Journal of Geophysical Research: Atmospheres, pp. 1–12, 2013.

Wang, Y., Cheng, H., Edwards, R. L., Kong, X., Shao, X., Chen, S., Wu, J., Jiang, X., Wang, X., and An, Z.: Millennial-and orbital-scale changes in the East Asian monsoon over the past 224,000 years, Nature, 451, 1090–1093, 2008.

Wang, Y., Jian, Z., and Zhao, P.: Extratropical modulation on Asian summer monsoon at precessional bands, Geophysical Research Letters, 39, 2012.

Weber, S. and Tuenter, E.: The impact of varying ice sheets and greenhouse gases on the intensity and timing of boreal summer monsoons, Quaternary Science Reviews, 30, 469–479, 2011.

Wu, C.-H., Lee, S.-Y., Chiang, J. C., and Hsu, H.-H.: The influence of obliquity in the early Holocene Asian summer monsoon, Geophysical Research Letters, 43, 4524–4530, 2016.

Zhao, Y., Braconnot, P., Marti, O., Harrison, S. P., Hewitt, C., Kitoh, A., Liu, A., Mikolajewicz, U., Otto-Bliesner, B., and Weber, S. L.: A multi-model analysis of the role of the ocean on the African and Indian monsoon during the mid-Holocene, Climate Dynamics, 25, 777–800, doi: 10.1007/s00382-005-0075-7, 2005.

Zheng, W., Wu, B., He, J., and Yu, Y.: The East Asian Summer Monsoon at mid-Holocene: results from PMIP3 simulations, Climate of the Past, 9, 453–466, doi:10.5194/cp-9-453-2013, URL http://www.clim-past.net/9/453/2013/, 2013.

Ziegler, M., Lourens, L. J., Tuenter, E., Hilgen, F., Reichart, G.-J., and Weber, N.: Precession phasing offset between Indian summer monsoon and Arabian Sea productivity linked to changes in Atlantic overturning circulation, Paleoceanography, 25, n/a–n/a, doi:10.1029/2009PA001884, URL http://dx.doi.org/10.1029/2009PA001884, 2010.

A Supplementary material: Choice of calendar

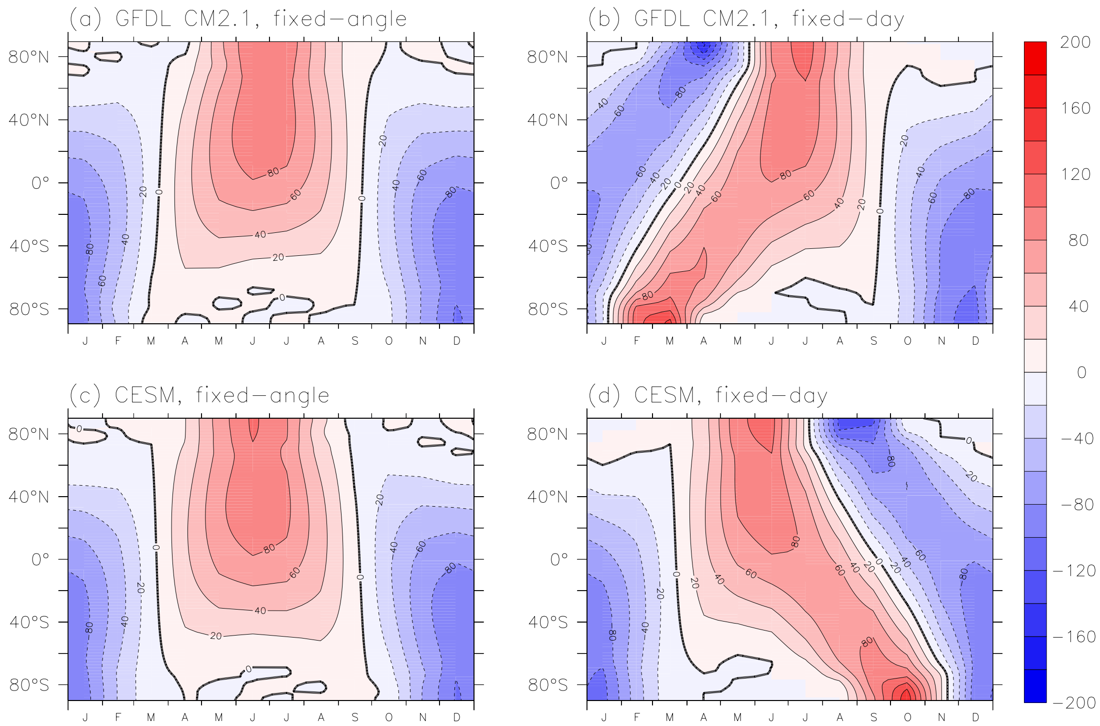

Figure A.1: Precession-induced insolation difference in W/m^2 (Pmin - Pmax) for GFDL (a,b) and CESM (c,d). The fixed-angle calendar used here is shown in (a,c), the original fixed-day calendar in (b,d). Results are converted to the fixed-angle calendar to align solstices and equinoxes throughout the year, but the choice of calendar does not change the conclusions discussed in this paper. Results in (b) and (d) look different primarily because the two models fix the calendar at different dates: the autumnal equinox for GFDL CM2.1 and the vernal equinox for CESM.

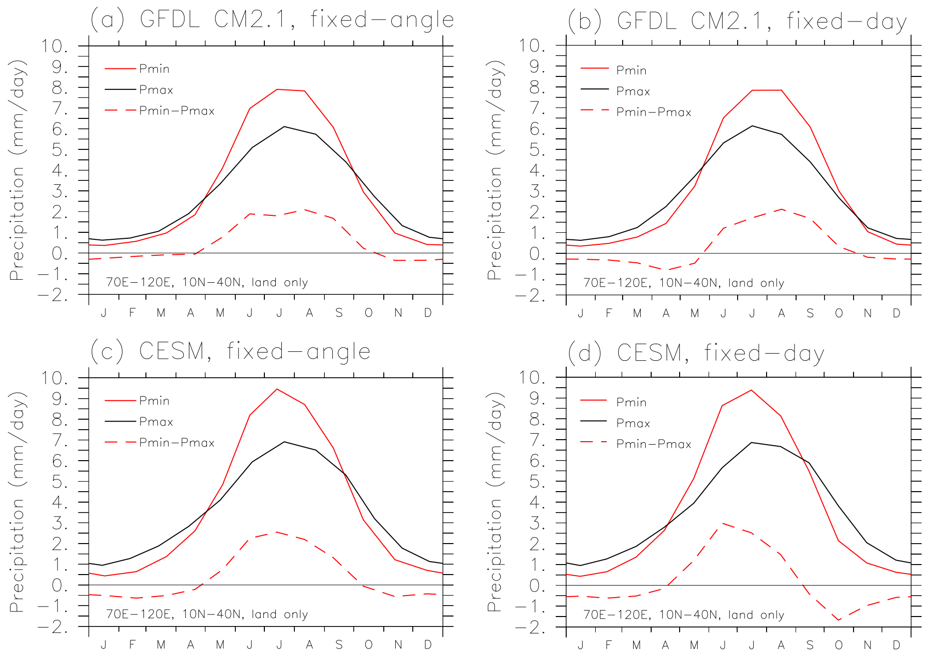

Figure A.2: Precipitation per month for GFDL (a,b) and CESM (c,d) precession experiments, on both the fixed-angle calendar (a,c) and the original fixed-day calendar (b,d) . Precipitation is given in mm/day averaged over the area 70°E-120°E, 10°N:40°N, using land grid cells only.

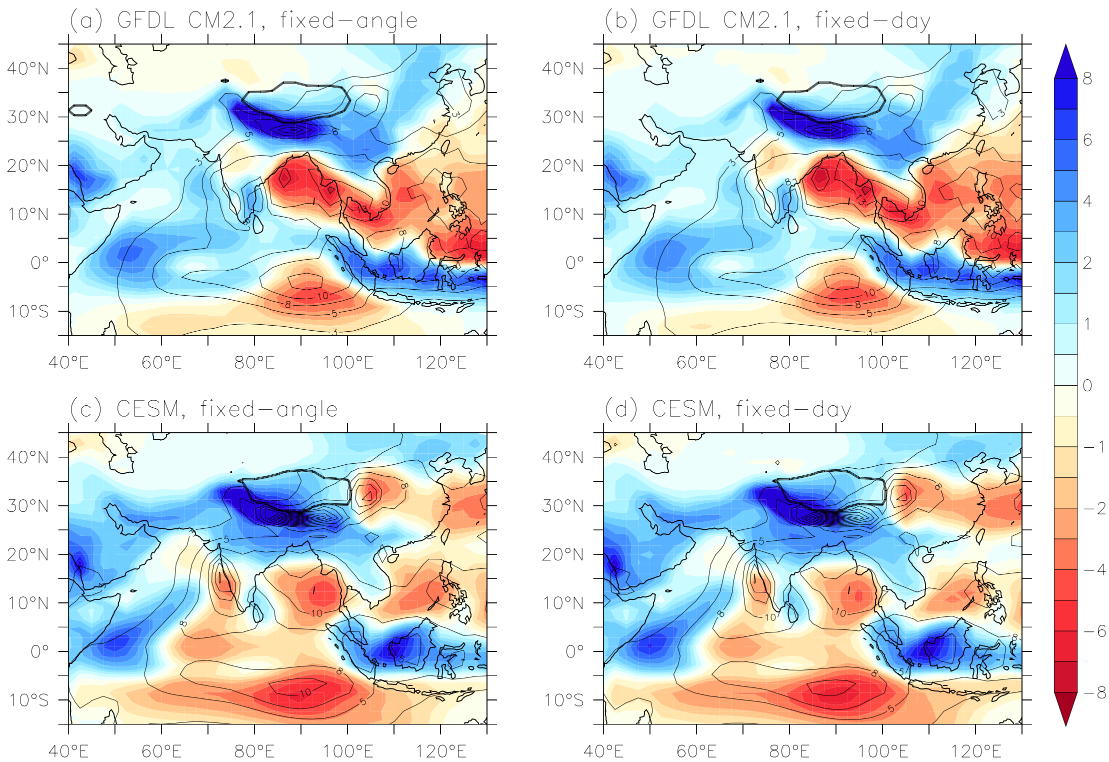

Figure A.3: June-July-August average precipitation difference for Pmin-Pmax for GFDL (a,b) and CESM (c,d). Contours indicate values for Pmax (left) in mm/day. The thick contour line is at 4km height, indicating the Tibetan Plateau. Panels (a,c) show the results on a fixed-angle calendar, and panels (b,d) show the results on the (original) fixed-day calendar.

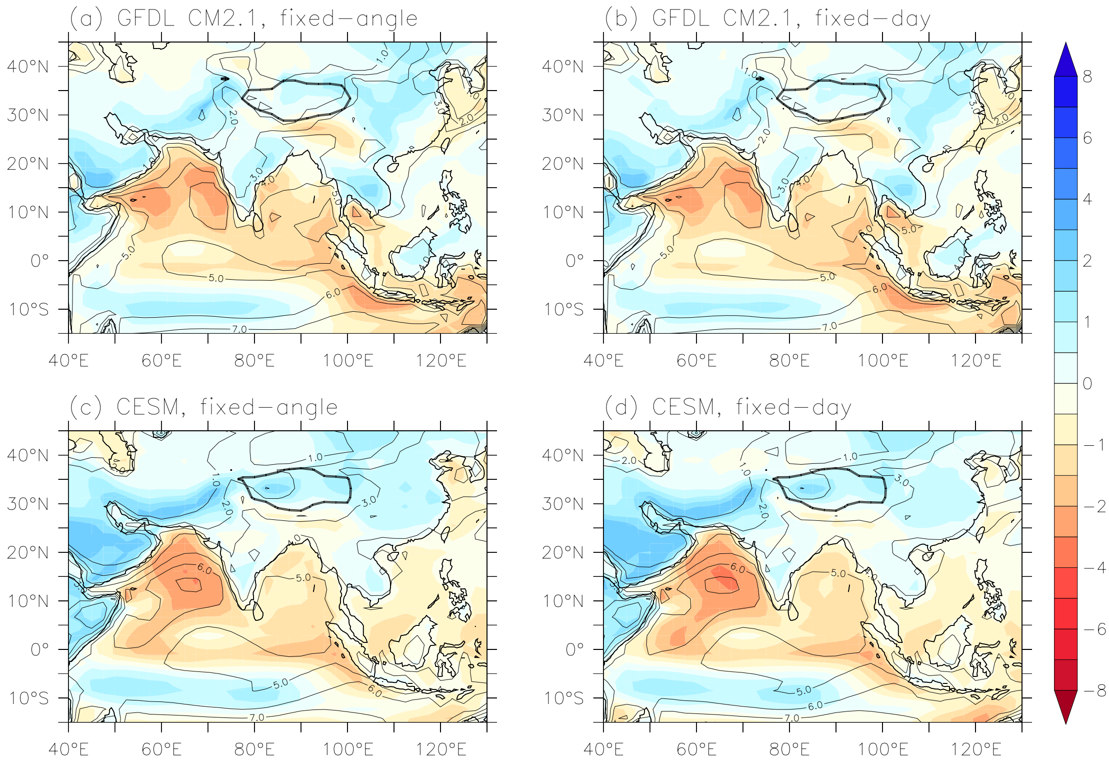

Figure A.4: June-July-August average evaporation difference for Pmin-Pmax for GFDL (a,b) and CESM (c,d). Contours indicate values for Pmax (left) in mm/day. The thick contour line is at 4km height, indicating the Tibetan Plateau. Panels (a,c) show the results on a fixed-angle calendar, and panels (b,d) show the results on the (original) fixed-day calendar.

B Supplementary material: Orography

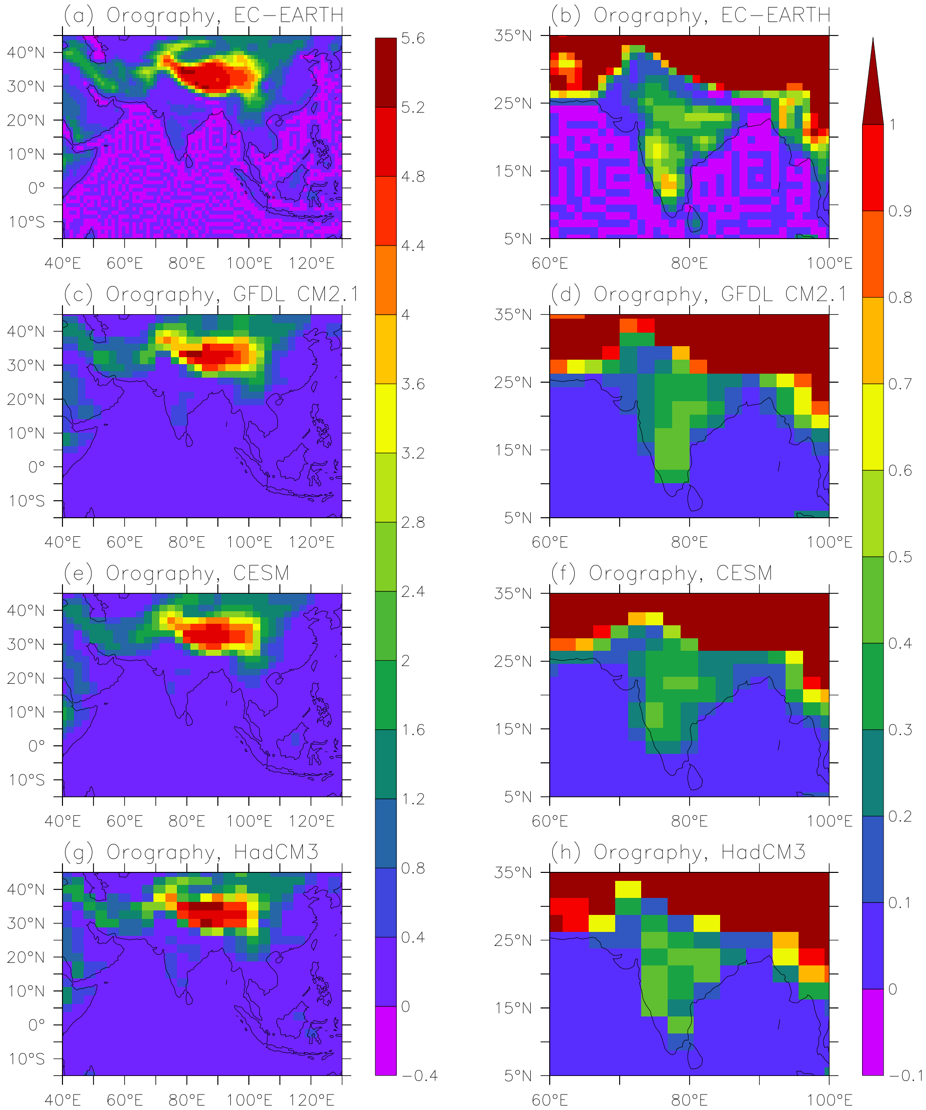

Figure B.1: Surface height in km in all models (orography) over the whole Asian area considered in this study (left) and over India (right). Note the different range in the colour bar left and right.

C Supplementary material: Results per model

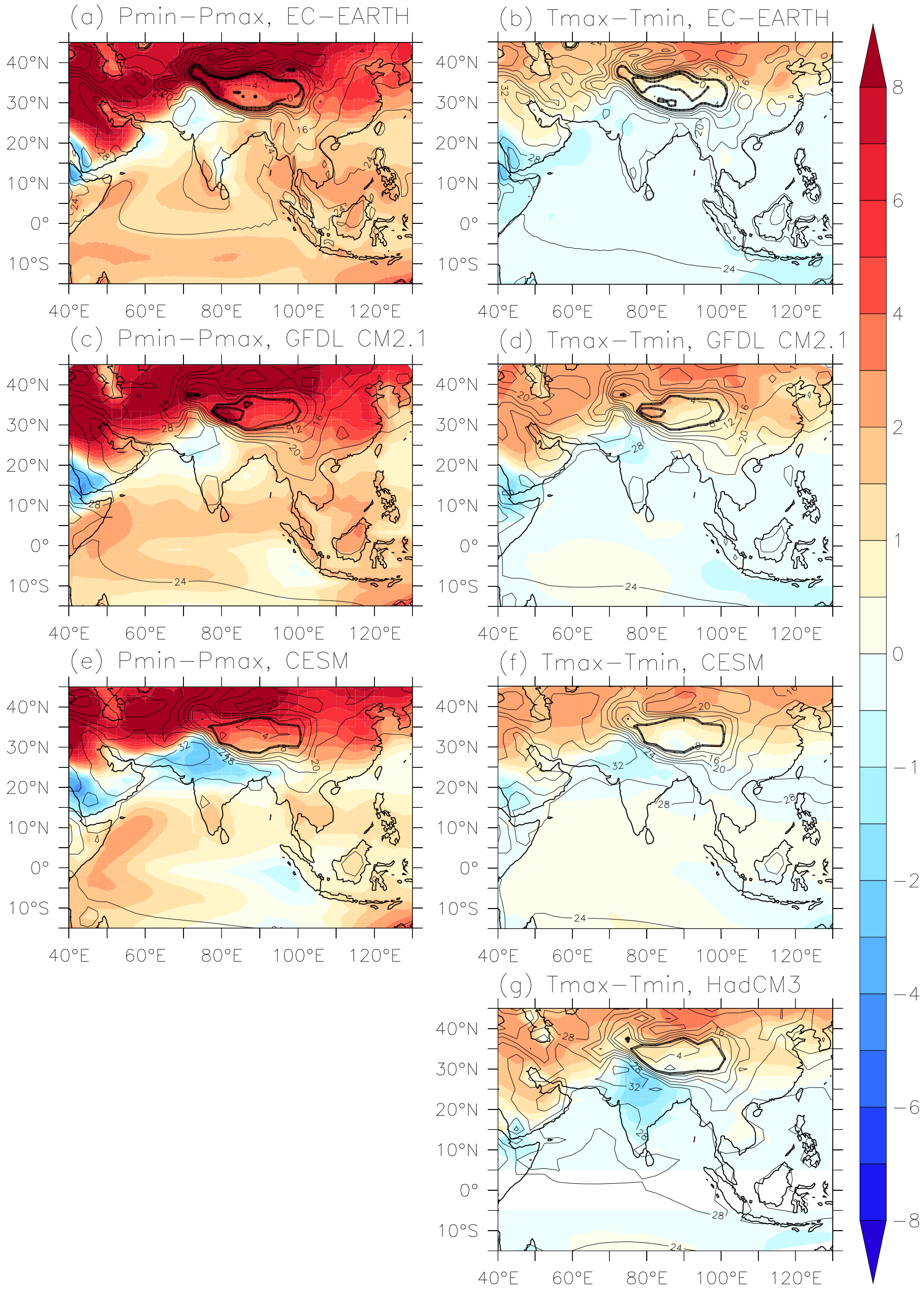

Figure C.1: June-July-August average surface air temperature difference for Pmin-Pmax (left) and Tmax-Tmin (right) for all models. Contours indicate values for Pmax (left) or Tmin (right) in °C. The thick contour line is at 4km height, indicating the Tibetan Plateau. Note that temperature is given at 2m above the surface, except for 1.5m in HadCM3. As in Figure 4 in the main text, but for all models.

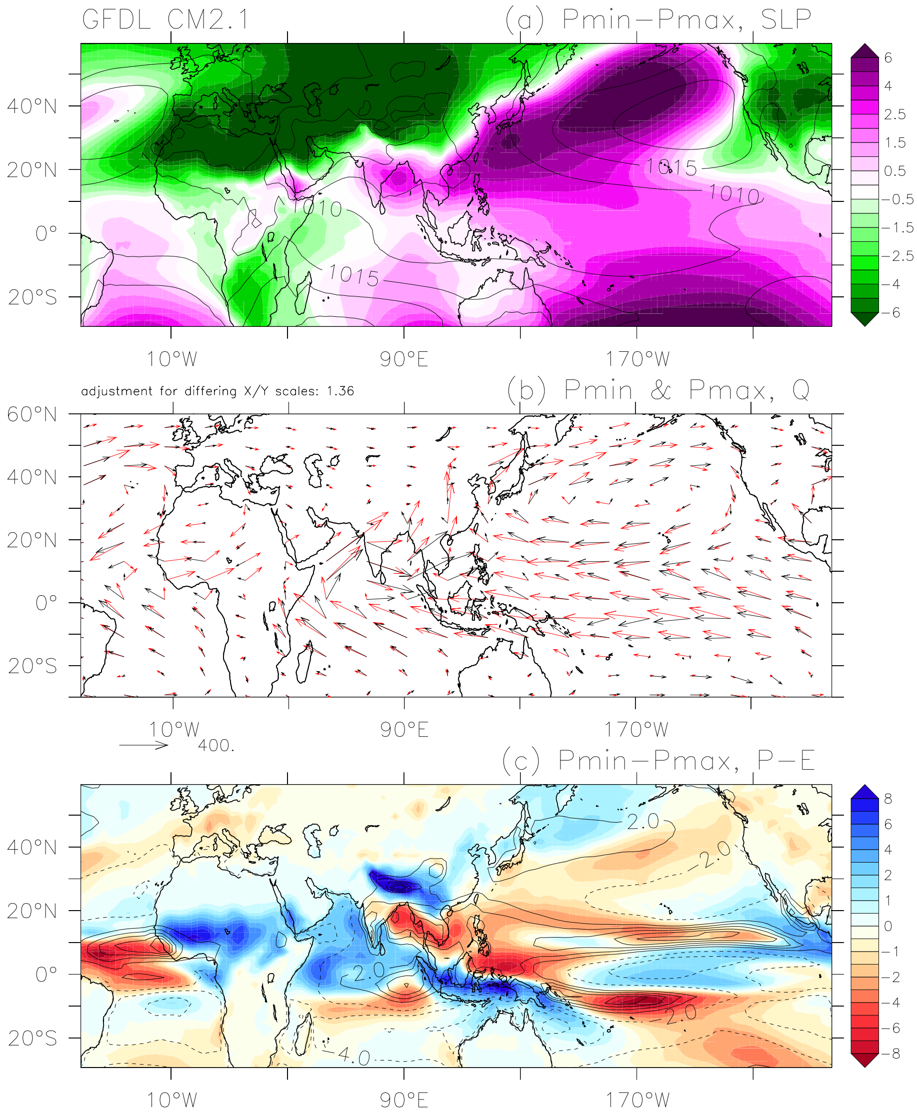

Figure C.2: June-July-August average results for GFDL Pmin-Pmax. Top (a) shows sea level pressure difference in hPa with Pmax values in contours. Middle (b) shows moisture transport **Q**, the vertical integral of q**v** in kg/(ms), during Pmin in red, and Pmax in black. Monthly model outputs are used. Bottom (c) shows net precipitation with positive values (blue) indicating increased net precipitation in mm/day and contours showing net precipitation during Pmax JJA.

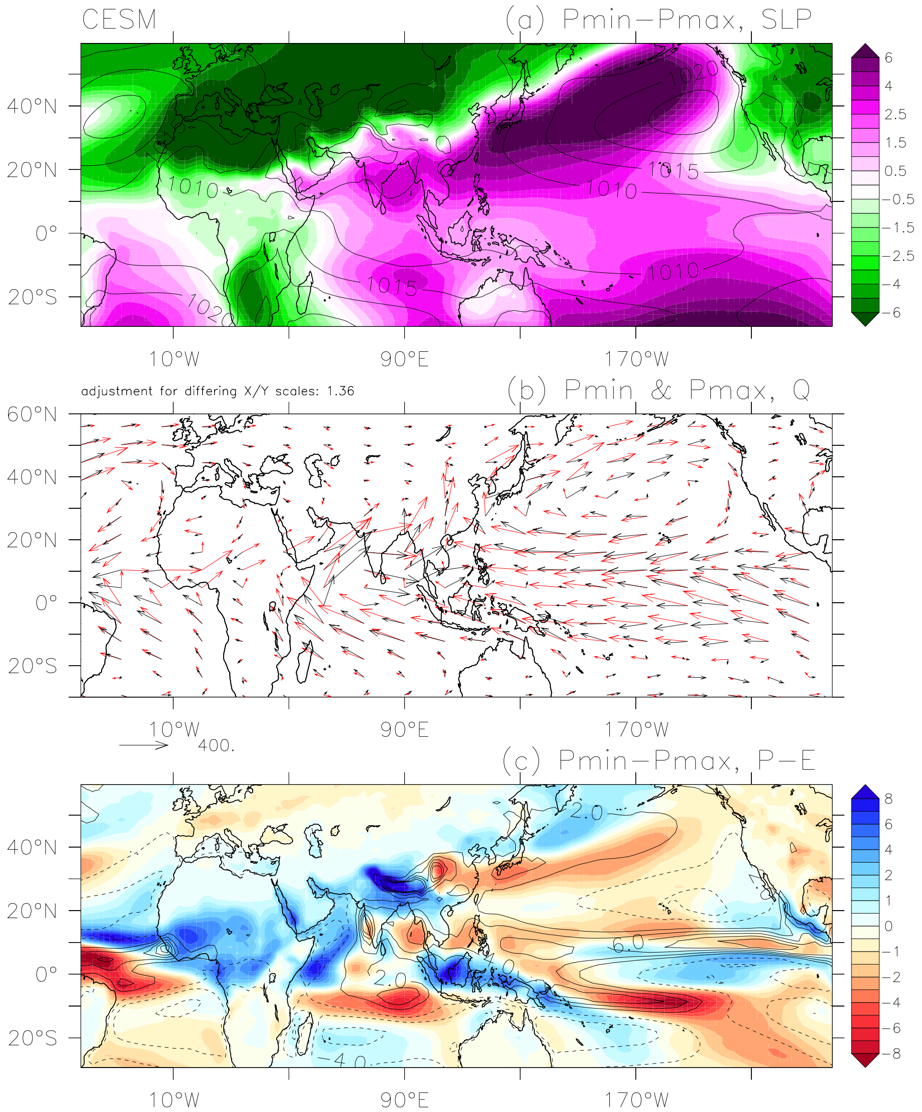

Figure C.3: June-July-August average results for CESM Pmin-Pmax. Top (a) shows sea level pressure difference in hPa with Pmax values in contours. Middle (b) shows moisture transport **Q**, the vertical integral of q**v** in kg/(ms), during Pmin in red, and Pmax in black. Monthly model outputs are used. Bottom (c) shows net precipitation with positive values (blue) indicating increased net precipitation in mm/day and contours showing net precipitation during Pmax JJA.

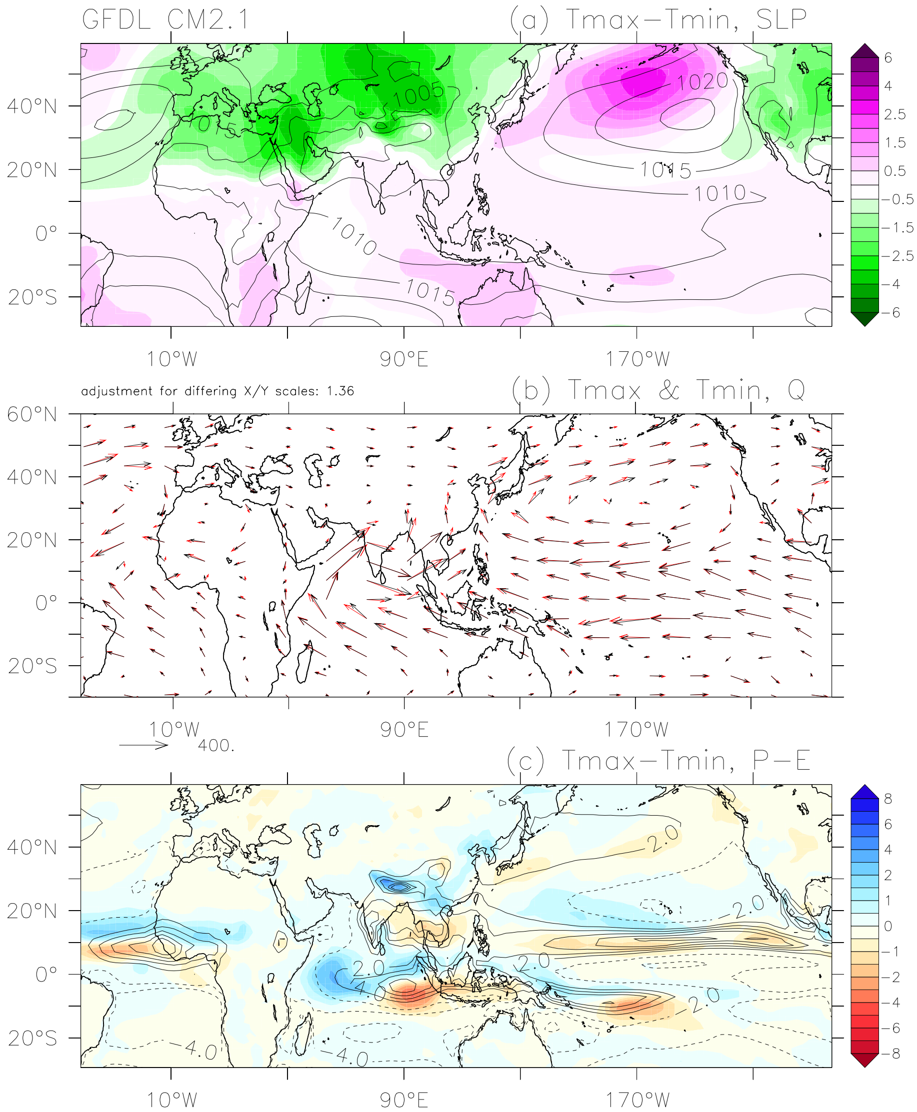

Figure C.4: June-July-August average results for GFDL Tmax-Tmin. Top (a) shows sea level pressure difference in hPa with Tmin values in contours. Middle (b) shows moisture transport **Q**, the vertical integral of q**v** in kg/(ms), during Tmax in red, and Tmin in black. Monthly model outputs are used. Bottom (c) shows net precipitation with positive values (blue) indicating increased net precipitation in mm/day and contours showing net precipitation during Tmin JJA.

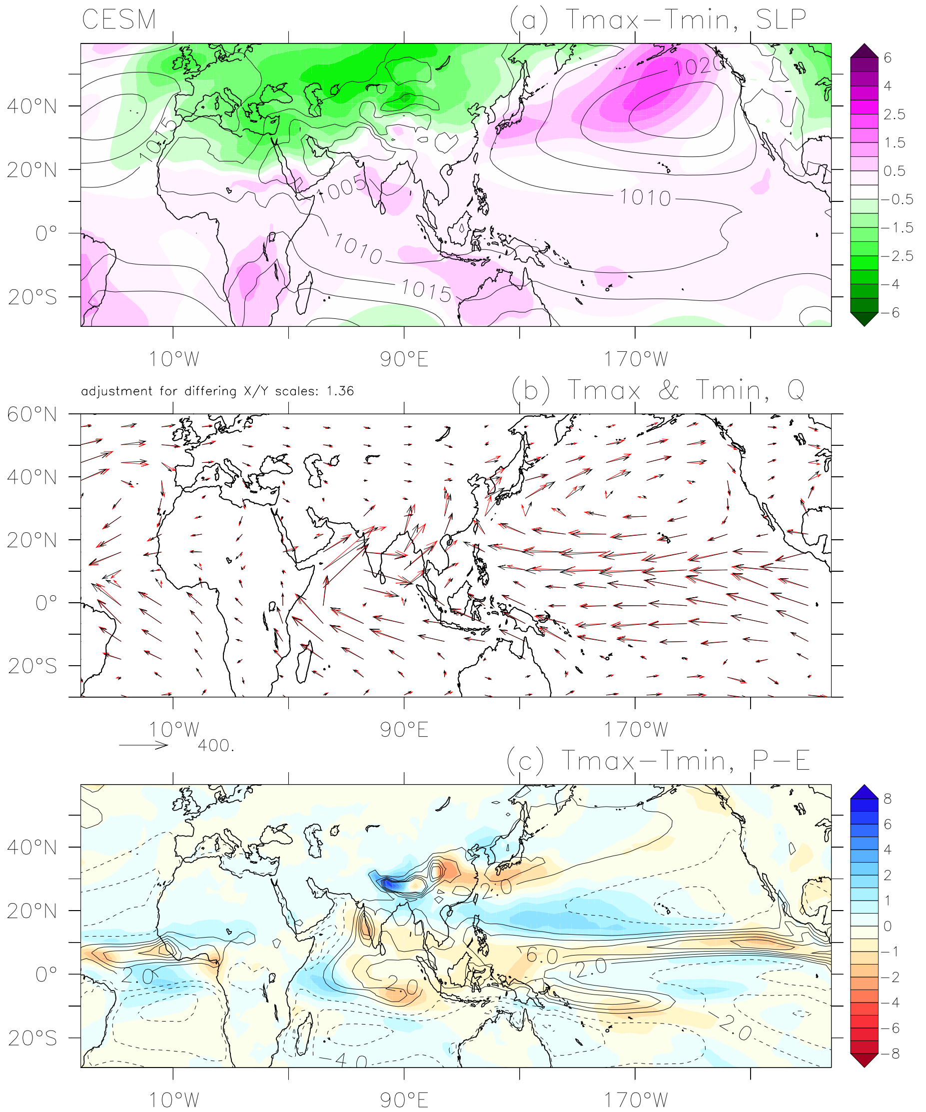

Figure C.5: June-July-August average results for CESM Tmax-Tmin. Top (a) shows sea level pressure difference in hPa with Tmin values in contours. Middle (b) shows moisture transport **Q**, the vertical integral of q**v** in kg/(ms), during Tmax in red, and Tmin in black. Monthly model outputs are used. Bottom (c) shows net precipitation with positive values (blue) indicating increased net precipitation in mm/day and contours showing net precipitation during Tmin JJA.

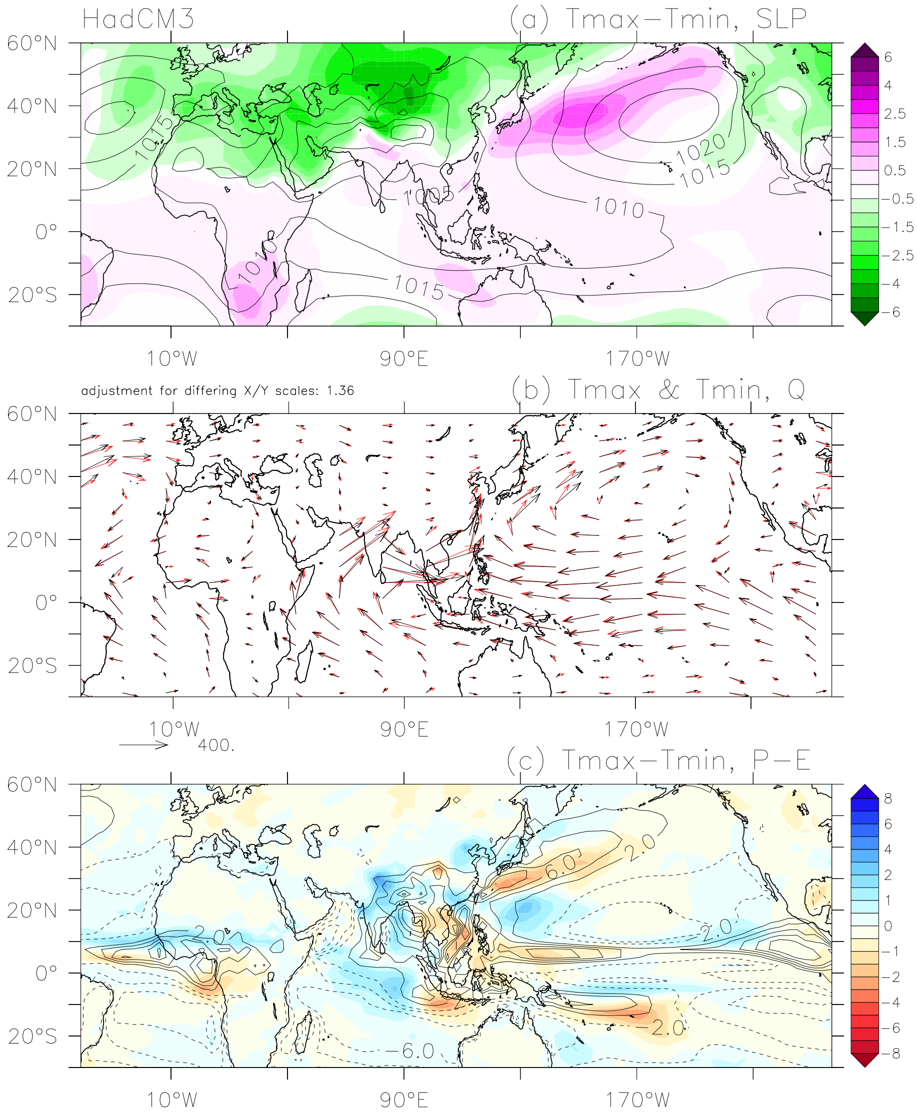

Figure C.6: June-July-August average results for HadCM3 Tmax-Tmin. Top (a) shows sea level pressure difference in hPa with Tmin values in contours. Middle (b) shows moisture transport **Q**, the vertical integral of q**v** in kg/(ms), during Tmax in red, and Tmin in black. Monthly model outputs are used. Bottom (c) shows net precipitation with positive values (blue) indicating increased net precipitation in mm/day and contours showing net precipitation during Tmin JJA.

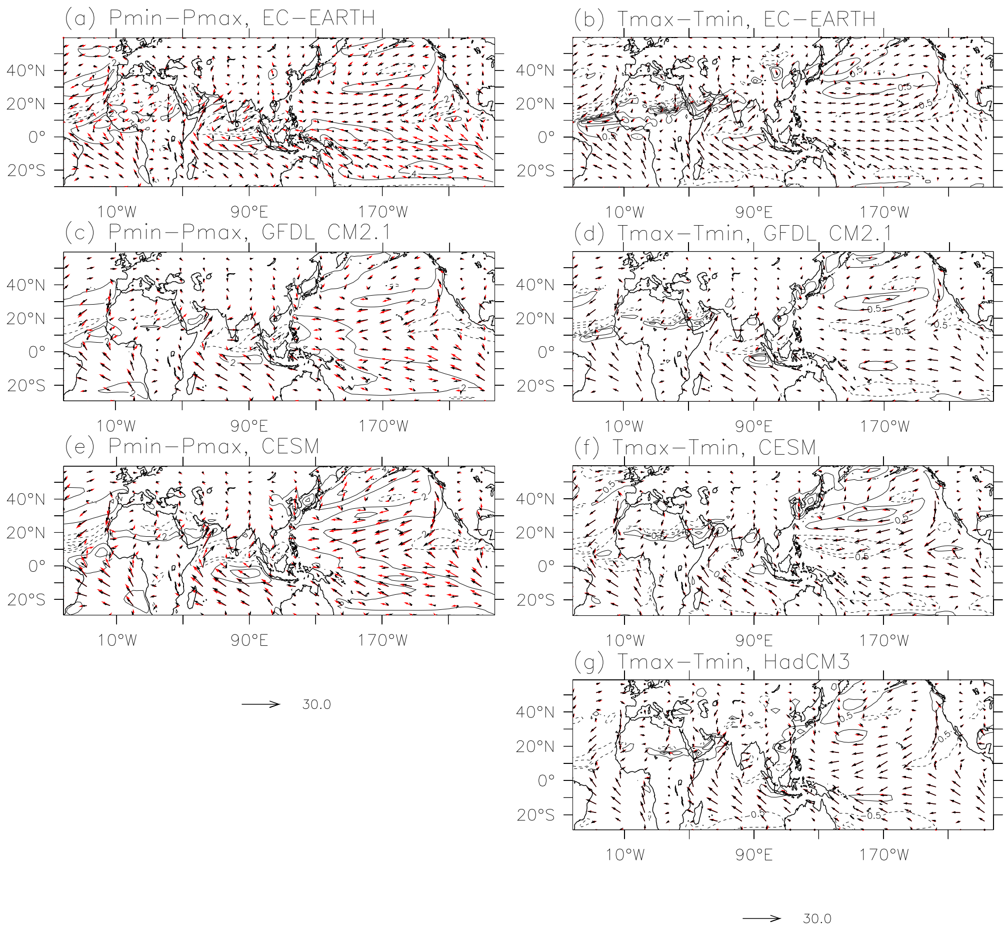

Figure C.7: June-July-August average surface wind in m/s for Pmin-Pmax (left) and Tmax-Tmin (right) for all models. Pmin is given in red, Pmax in black, Tmax in green and Tmin in blue. Contours indicate wind speed differences for Pmin-Pmax (left) and Tmax-Tmin (right), with contour levels set to 2 m/s on the left and 0.5 m/s on the right. Unit length is 30 m/s. Note that wind speed is given at 10m above the surface, except for CESM where only the lowest model level was available, on average 66m above the surface. As in Figure 7 in the main text, but for all models.

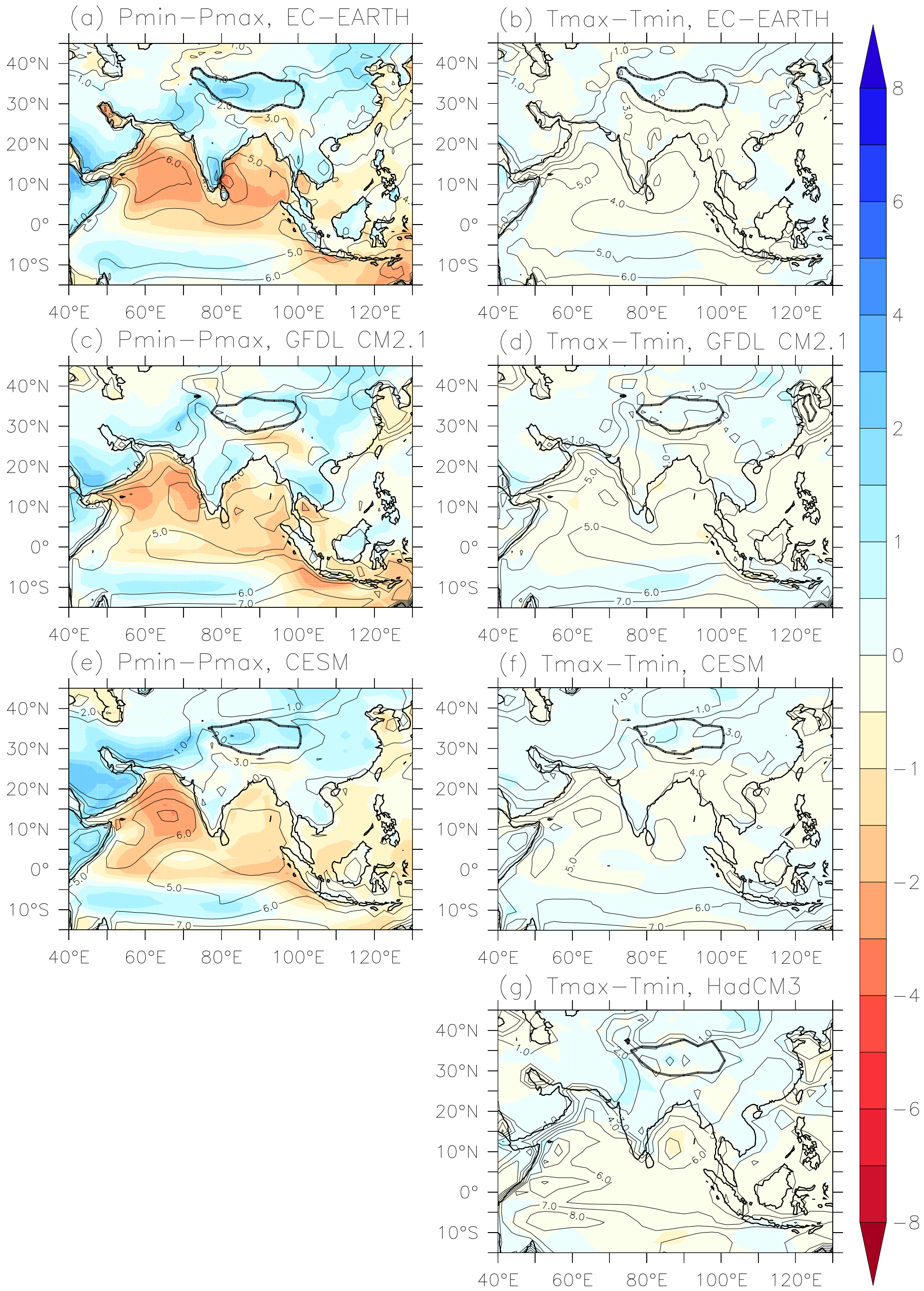

Figure C.8: June-July-August average evaporation difference in mm/day for Pmin-Pmax (left) and Tmax-Tmin (right) for all models. Contours indicate values for Pmax (left) or Tmin (right). The thick contour line is at 4km height, indicating the Tibetan Plateau. As in Figure 8 in the main text, but for all models.

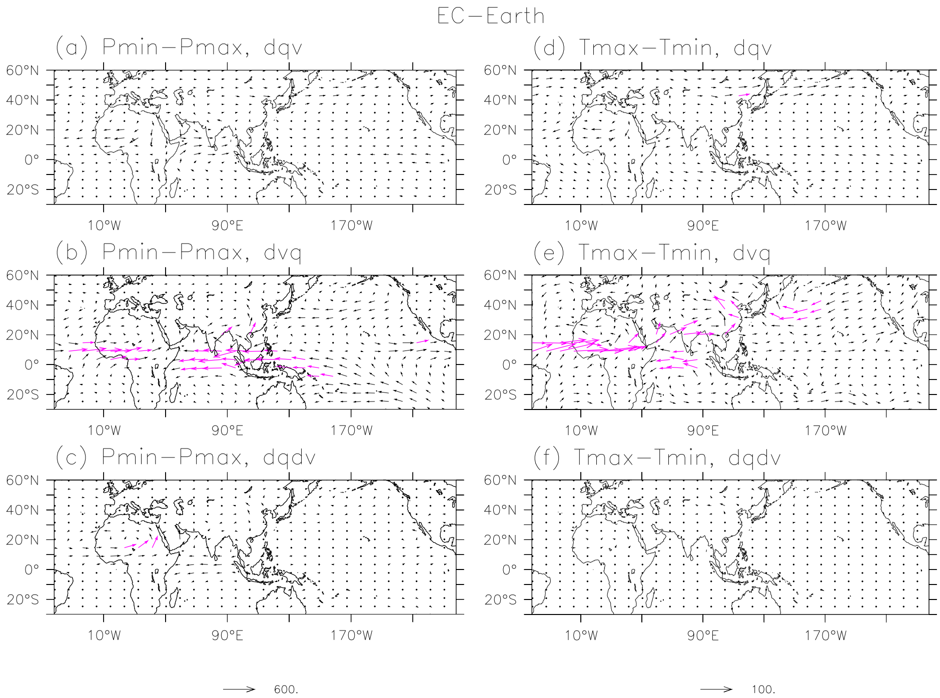

Figure C.9: Breakdown of June-July-August average moisture transport changes d**Q**, the vertical integral of d(q**v**) in kg/(ms), for precession (Pmin-Pmax, left) and obliquity (Tmax-Tmin, right) in EC-Earth. d**Q** is broken down following Equation 1 in (Bosmans et al., 2015a) into dq**v** (top, the thermodynamic part, related to changes in specific humidity, with Pmax **v**), d**v**q (middle, the dynamic part, related to changes in wind, with Pmax q) and dqd**v** (bottom, due to changes in both humidity and wind). Unit vector length for precession (left) is 600, with purple vectors indicating vectors larger than 200. For obliquity (right), vector length is 100, with purple vectors indicating changes in moisture transport larger than 30 kg/(ms). For these breakdown terms, monthly model output was used. The total moisture transport **Q** for EC-Earth is given in Figures 5, 6.

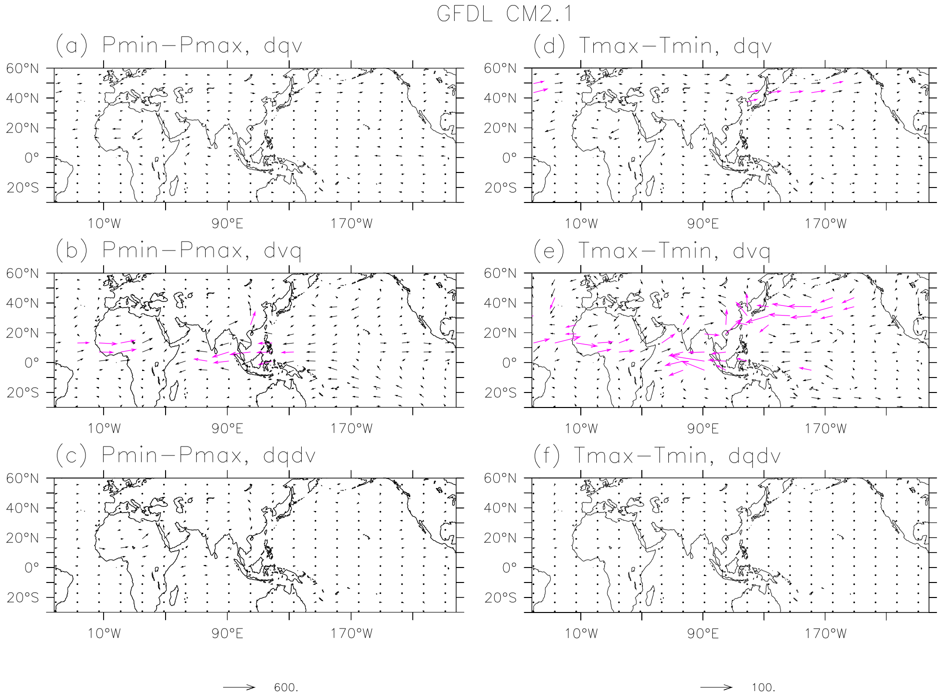

Figure C.10: Breakdown of June-July-August average moisture transport changes d**Q**, the vertical integral of d(q**v**) in kg/(ms), for precession (Pmin-Pmax, left) and obliquity (Tmax-Tmin, right) in GFDL. d**Q** is broken down following Equation 1 in (Bosmans et al., 2015a) into dq**v** (top, the thermodynamic part, related to changes in specific humidity, with Pmax **v**), d**v**q (middle, the dynamic part, related to changes in wind, with Pmax q) and dqd**v** (bottom, due to changes in both humidity and wind). Unit vector length for precession (left) is 600, with purple vectors indicating vectors larger than 200. For obliquity (right), vector length is 100, with purple vectors indicating changes in moisture transport larger than 30 kg/(ms). For these breakdown terms, monthly model output was used. The total moisture transport **Q** for GFDL is given in Figures C.2, C.4.

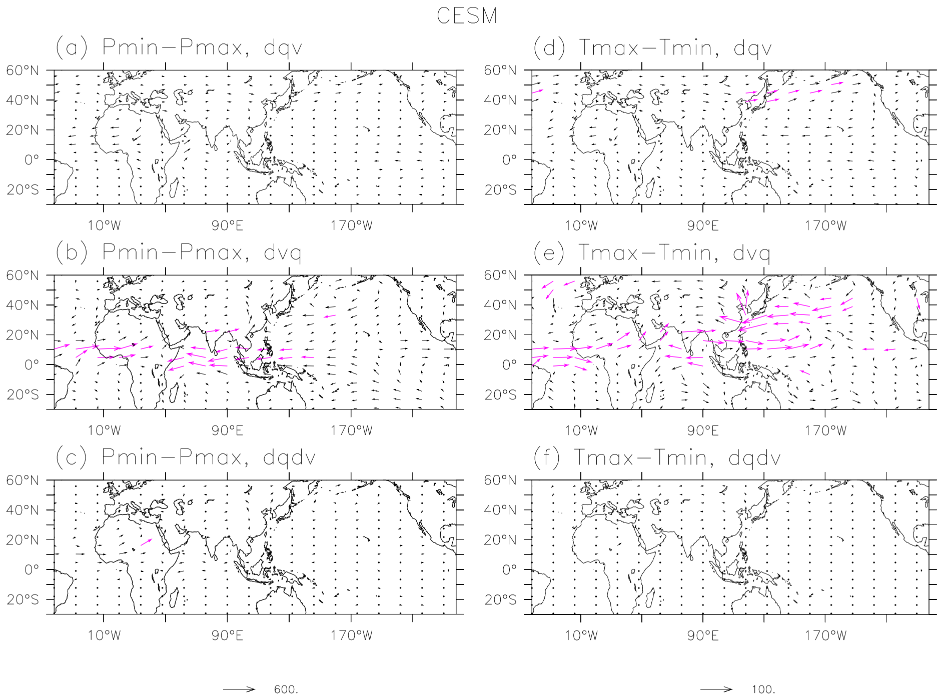

Figure C.11: Breakdown of June-July-August average moisture transport changes d**Q**, the vertical integral of d(q**v**) in kg/(ms), for precession (Pmin-Pmax, left) and obliquity (Tmax-Tmin, right) in CESM. d**Q** is broken down following Equation 1 in (Bosmans et al., 2015a) into dq**v** (top, the thermodynamic part, related to changes in specific humidity, with Pmax **v**), d**v**q (middle, the dynamic part, related to changes in wind, with Pmax q) and dqd**v** (bottom, due to changes in both humidity and wind). Unit vector length for precession (left) is 600, with purple vectors indicating vectors larger than 200. For obliquity (right), vector length is 100, with purple vectors indicating changes in moisture transport larger than 30 kg/(ms). For these breakdown terms, monthly model output was used. The total moisture transport **Q** for CESM is given in Figures C.3, C.5.

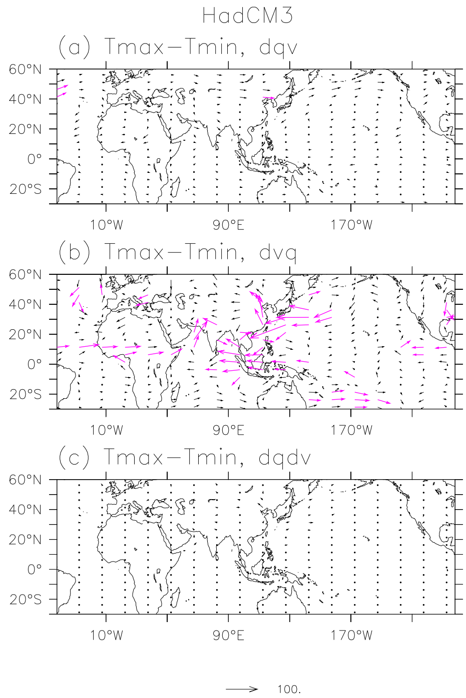

Figure C.12: Breakdown of June-July-August average moisture transport changes d**Q**, the vertical integral of d(q**v**) in kg/(ms) for obliquity (Tmax-Tmin) in HadCM3. d**Q** is broken down following Equation 1 in (Bosmans et al., 2015a) into dq**v** (top, the thermodynamic part, related to changes in specific humidity, with Pmax **v**), d**v**q (middle, the dynamic part, related to changes in wind, with Pmax q) and dqd**v** (bottom, due to changes in both humidity and wind). Unit vector length for obliquity is 100, with purple vectors indicating changes in moisture transport larger than 30 kg/(ms). For these breakdown terms, monthly model output was used. The total moisture transport **Q** for HadCM3 is given in Figure C.6.

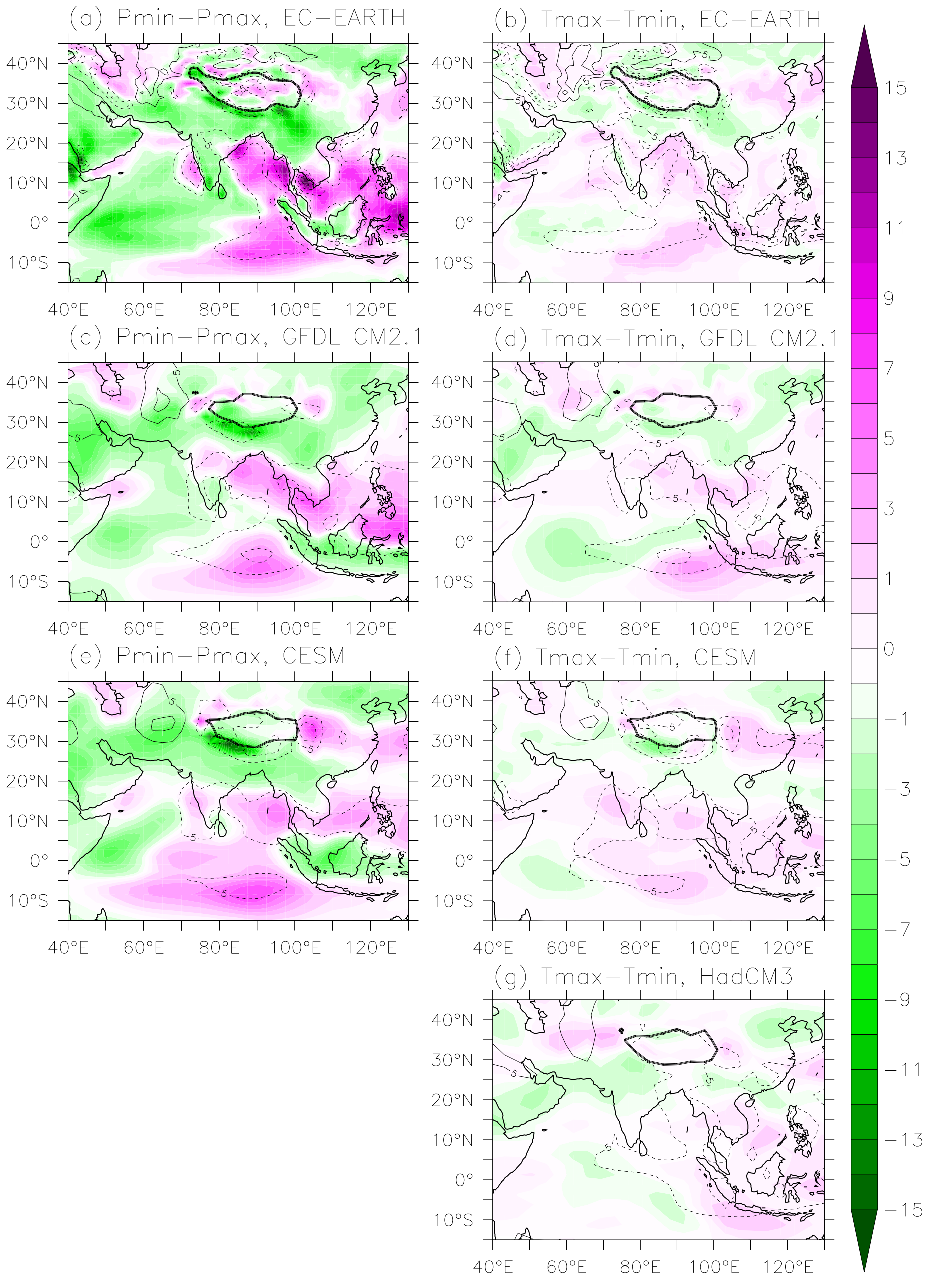

Figure C.13: June-July-August average vertical velocity at 500 hPa in 10^{-2}Pa/s for Pmin-Pmax (left) and Tmax-Tmin (right) for all models. Contours indicate values for Pmax (left) or Tmin (right) with negative values indicating upward motion. Green indicates more upward or less downward motion, purple indicates more downward or less upward motion. The thick contour line is at 4km height, indicating the Tibetan Plateau. As in Figure 9 in the main text, but for all models.

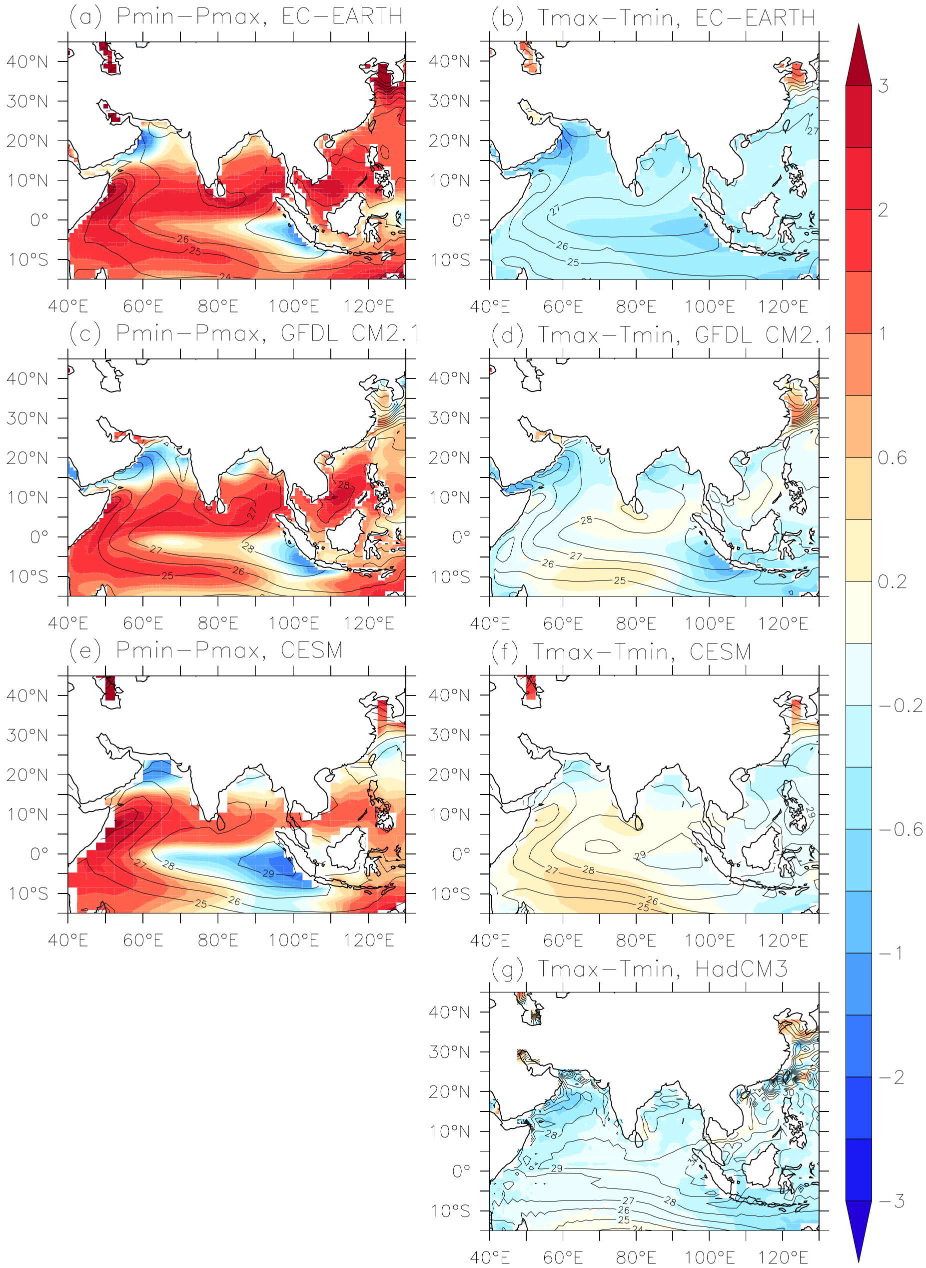

Figure C.14: June-July-August average sea surface temperature difference for Pmin-Pmax (left) and Tmax-Tmin (right) for all models. Contours indicate values for Pmax (left) or Tmin (right) in °C. As in Figure 10 in the main text, but for all models.